JGR Planets

RESEARCH ARTICLE

10.1029/2025JE009024

Fluid Flow at the Top of Jupiter's Dynamo Region

S. Sharan[1], M. A. Pais[2], H. Amit[3], and B. Langlais[3]

[1]Blackett Laboratory, Department of Physics, Imperial College London, London, UK, [2]Department of Physics, University of Coimbra, CITEUC, Coimbra, Portugal, [3]Laboratoire de Planétologie et Géosciences, CNRS UMR 6112, Nantes Université, Université d'Angers, Le Mans Université, Nantes, France

Key Points:

- First inversions of high-resolution secular variation models are performed for Jovian interior flows
- Flows display both meridional and azimuthal components of the order of a few 100 km/yr
- Jovian secular variation originates possibly due to flows powered in its interior as opposed to atmospheric zonal winds

Correspondence to:

S. Sharan,
s.sharan@imperial.ac.uk

Citation:

Sharan, S., Pais, M. A., Amit, H., & Langlais, B. (2025). Fluid flow at the top of Jupiter's dynamo region. *Journal of Geophysical Research: Planets*, *130*, e2025JE009024. https://doi.org/10.1029/2025JE009024

Received 27 FEB 2025
Accepted 3 DEC 2025

Abstract The magnetic main field (MF) and secular variation (SV) models for Jupiter can be used to gain insights about the internal dynamo and the flow that drives the field. We use two such models computed from Juno observations up to spherical harmonic degrees 16 and 8 for the MF and SV, respectively. We solve the radial magnetic induction equation in the frozen-flux approximation at the dynamo region outer boundary assuming zero radial velocity for four large-scale physical flow assumptions- unconstrained, toroidal, tangentially geostrophic and columnar. We find flows with root mean square velocity varying between 100 and 400 km/yr (0.3–1.3 cm/s) when the dynamo region spherical boundary is taken at 0.83 Jupiter radius. Equatorially symmetric, toroidal and non-zonal velocity components are larger than the anti-symmetric, poloidal and zonal components, respectively, for almost all cases. Toroidal and tangentially geostrophic flows display similar velocity values and patterns, despite relying on different physical assumptions. The four inverted solutions indicate that the Jovian interior has dominant eastward flows near the Great Blue Spot, in agreement with previous studies. In addition, our more complex flow models shed light on some new features such as a large non-zonal component, meridional flows in the southern hemisphere and field-aligned flows in the north. Finally, our unconstrained flow solution suggests upwelling near the south pole, consistent with thermal wind theory.

Plain Language Summary The temporal evolution of the main magnetic field of the Earth provides vital information on the fluid motion at the top of Earth's metallic outer core. We perform a similar inversion for the Jovian dynamo region using two models estimated from recent Juno magnetic observations. We benefit from their detailed description of relatively small lengthscales. However, different geometries of the metallic hydrogen convective currents inside the planet may give rise to the same observed planetary magnetic field outside Jupiter. We test different physically admissible flow models and obtain corresponding solutions for the velocity in Jupiter's interior. The root mean square velocities of the metallic hydrogen in the interior of Jupiter, at the top of the dynamo region, reach about 100–400 km/yr (0.3–1.3 cm/s). Our solutions display rich behavior in the interior that includes strong eastward advection near the intense negative field patch called the Great Blue Spot (GBS), strong equatorward meridional flow in the southern hemisphere, and an overall more vigorous convection in the southern than in the northern hemispheres with evidence of warm-fluid upwelling near the south pole.

1. Introduction

The large-scale and (relatively) slowly varying magnetic field in planetary bodies originates from a dynamo, a process that is sustained by convection of an electrically conducting liquid inside the rapidly rotating planet. Fluid flow in this dynamo region gives rise to time variations of the main field (MF), termed secular variation (SV), which can be monitored on and above the planet's surface. Our main reference to invert Jupiter's MF and SV models for internal flows is the Earth. For the Earth, abundant data from both ground and satellite observations allow to model the magnetic field and its evolution with increasingly high spatial and temporal resolution (e.g., Lesur et al., 2022). Geomagnetic SV models have been used to image the core flow that sustains the geodynamo (e.g., Bloxham & Jackson, 1991; Finlay et al., 2023; Gillet et al., 2019; Hulot et al., 2002; Pais & Jault, 2008). The flow solution is derived from the radial induction equation that relates the radial magnetic field and the horizontal velocity of an electrically conductive fluid at the top of the dynamo region, resorting to different physical assumptions to reduce the inherent non-uniqueness in the inverse problem (e.g., Holme, 2015).

Recent studies of Jupiter's magnetic field highlighted observations of strong SV ($\sim 10^3 - 10^4$ nT/yr at Jupiter's surface) (e.g., Moore et al., 2019; Sharan et al., 2022a). However, these models have not yet been used to derive

Jupiter's global distribution of both meridional and latitudinal flows at the top of the dynamo region. To our best knowledge, the only study that performed such a global inversion is that of Ridley and Holme (2016). They used Pioneer, Voyager, Ulysses and Galileo measurements to invert for the flow using the frozen-flux approximation, after computing MF and SV models reliable up to degrees 5 and 2, respectively. Two flow assumptions were considered, tangentially geostrophic and toroidal, which displayed similar velocities and patterns for some damping levels. They found flow magnitudes of about 200 km/yr close to the equator.

Alternatively, regional analyses of the SV in the vicinity of the Great Blue Spot (GBS, an intense patch of inward magnetic flux near the planet's equator) were performed. From a comparison of magnetic field observations from early space missions with a model computed from Juno first orbits, Moore et al. (2019) inverted for purely zonal flows and concluded that the SV of the GBS arises from eastward zonal winds at Jupiter's surface that can penetrate down to 0.95 R_J (Galanti et al., 2021; Kaspi et al., 2018). Connerney et al. (2022) compared two different MF models derived from Juno data with a time difference of 1.75 years. They reported a displacement of the GBS by 2,500 km in the eastward direction, in agreement with the results of Moore et al. (2019). Bloxham et al. (2022) interpreted the SV computed from Juno data in terms of a steady purely zonal flux velocity advecting the magnetic field. Their updated model with data from more orbits displayed poorer fits which led them to test a sinusoidally varying zonal flow (Bloxham et al., 2024). They found the best fit to the jet fluctuation for an approximately 4 years period. Furthermore, there have been some numerical magnetohydrodynamic simulations that related the strong zonal jets in Jupiter's atmosphere to the magnetic field and its SV. Cao and Stevenson (2017) proposed that deep zonal winds induce a poloidal magnetic field pattern spatially correlated with the zonal flow, while Wicht and Christensen (2024) suggested that deep zonal winds attenuate the non-axisymmetric field. As a result of the latter, the atmospheric zonal jets should penetrate only to relatively shallow depths in order to be compatible with the non-axisymmetric magnetic flux features observed on the surface, such as the GBS.

Higher resolution models of the Jovian MF and SV may improve the imaging of the flow at Jupiter's deep interior. Sharan et al. (2022a) modeled simultaneously the MF and SV using Juno magnetometer measurements along 28 orbits. They obtained reliable models up to spherical harmonic degrees (n) 16 and 8, respectively. Based on the white noise hypothesis for the power spectra obtained from the non-zonal ($m \neq 0$) and quadrupole ($n + m$ even) families of the MF G coefficients (Langlais et al., 2014), they proposed that the Jovian dynamo resides below about 0.83 R_J (1 R_J = 71,492 km). Furthermore, based on the degree dependence of the SV timescales, Sharan et al. (2022a) argued that the Jovian SV is dominated by advection of the magnetic field by fluid flow of metallic hydrogen. They observed that the SV spectra increase with degree at both the surface and dynamo radius, while the SV patterns at the dynamo radius show various interesting small-scale features: (a) an eastward drift is inferred for the so-called GBS from a pair of SV patches of opposite signs; (b) similar eastward drift is suggested for the eastern edge of a large intense patch of positive flux in the northern hemisphere near 45°N latitude; (c) overall, weak SV near this large northern magnetic flux patch is suggestive of weak or field-aligned flows there; (d) in addition, opposite signs of field and SV near the south pole may suggest local fluid upwelling (Sharan et al., 2022a). Sharan (2023) updated this model using observations from 10 more recent Juno orbits. The new model displays similar features of the SV as well as the same dynamo radius and dominant advection effects, demonstrating the robustness of the models that explain the magnetic field of Jupiter and its temporal changes. Nevertheless, the new SV model of Sharan (2023) differs from that of Sharan et al. (2022a) in some local features, which we describe in a later section.

It is important to unravel the flow at the top of the dynamo region of Jupiter, from existing observations, in order to constrain the planet's internal dynamics. While most studies attribute Jupiter's main SV features to field advection by zonal flows (e.g., Bloxham et al., 2022, 2024; Moore et al., 2019), there has been no global flow inversions using reliable high resolution SV models in an analogous way to that commonly done for the Earth. Therefore, in this work, we use Jupiter's MF and SV models with spatial resolution up to spherical harmonic degrees 16 and 8, respectively, and a flow parameterization that allows for more complex behavior while still compatible with observations, in an effort to provide a constraint on the Jovian dynamo. Section 2 describes the theory and Section 3 presents the input models. The method, including the different physical assumptions that are used for the inversion, are described in Section 4. Section 5 displays the results for the different flow solutions and we discuss our findings in Section 6. We end with our main conclusions in Section 7.

2. Theory

Here we recall the derivation of the frozen-flux radial magnetic induction equation at the top of the dynamo region. We point out the two assumptions commonly used in the context of the flow right below the Earth's core-mantle boundary: zero radial flow and flow incompressibility. If zero radial flow is not a valid assumption, which may be the case for the top of the dynamo region in Jupiter's interior, some additional terms should be retained. We derive and present these terms here. We also show that the frozen-flux radial induction equation is identical for both compressible and incompressible flows, though the physical meaning of the horizontal divergence differs in the two cases.

Given the high electrical conductivity of the Earth's core fluid, on short timescales and large length scales the geomagnetic SV is mostly induced by the transport of magnetic field lines by the flow (Roberts & Scott, 1965). This frozen-flux hypothesis is justified for the Earth's outer core because the magnetic Reynolds number (R_m), which represents the ratio of advection to magnetic diffusion effects, is very large (∼1000, e.g., Christensen et al., 2010). Such an estimate for the Earth's outer core is robust because the characteristic length scale (outer core thickness) is known from seismology, the typical flow velocity is inferred from tracing mobile geomagnetic flux patches over the period of historical observations and the magnetic diffusivity of molten iron is estimated from high pressure mineral physics experiments (e.g., Holme, 2015). However, it is difficult to estimate R_m for Jupiter. First, the period of direct observations is too short for a robust evaluation of the velocity from the displacement of the MF features. Second, the thickness of the Jovian dynamo region is uncertain. Nevertheless, considering a fraction of the planet radius as a characteristic lengthscale (e.g., 0.1 R_J), velocity estimates of ∼4 cm/s for the GBS drift from recent Juno data (Connerney et al., 2022), and an electrical conductivity $\sim 10^3 - 10^5$ Sm^{-1} for metallic hydrogen inside Jupiter (French et al., 2012) provides $R_m \sim 10^2 - 10^4$. Furthermore, there are also other observations which support the frozen-flux hypothesis. The slope of the SV timescales (τ_{SV}) versus spherical harmonic degree n indicates either SV dominated by advection ($\tau_{SV} \propto n^{-1}$ for non dipole terms) or by diffusion ($\tau_{SV} \propto n^{-2}$ for non dipole terms). The approximately −1 slope of the non-dipole Jovian SV timescales versus spherical harmonic degree (Sharan et al., 2022a) suggests that advection is dominant inside the dynamo region (Christensen et al., 2012), as in the Earth's core (e.g., Amit et al., 2018; Bouligand et al., 2016; Lhuillier et al., 2011) and R_m should be large (∼1,000 as for Earth) (Christensen & Tilgner, 2004). In both cases, R_m is significantly large, hence, we apply the frozen-flux approximation for Jupiter.

Following this approximation, the magnetic induction equation is

$$\frac{\partial \mathbf{B}}{\partial t} = \nabla \times (\mathbf{u} \times \mathbf{B}) \tag{1}$$

where $\mathbf{B}$ is the magnetic field vector, $\mathbf{u}$ is the fluid velocity vector and t is time. The radial component of the frozen-flux induction equation is

$$\frac{\partial B_r}{\partial t} = (\mathbf{B} \cdot \nabla) u_r - (\mathbf{u} \cdot \nabla) B_r - B_r(\nabla \cdot \mathbf{u}) \tag{2}$$

where B_r and u_r represent the radial components of the magnetic field and flow, respectively. Both for incompressible and compressible flows, Equation 2 can be rewritten as

$$\frac{\partial B_r}{\partial t} = (\mathbf{B}_h \cdot \nabla_h) u_r - B_r \left[(\nabla_h \cdot \mathbf{u}_h) + 2\frac{u_r}{r} \right] - u_r \frac{\partial B_r}{\partial r} - (\mathbf{u}_h \cdot \nabla_h) B_r \tag{3}$$

where the horizontal magnetic field and flow vectors are $\mathbf{B}_h = B_\theta \hat{\theta} + B_\phi \hat{\phi}$ and $\mathbf{u}_h = u_\theta \hat{\theta} + u_\phi \hat{\phi}$, respectively, and $\nabla = \nabla_h + \hat{r}\partial/\partial r$. θ and ϕ represent the co-latitude and longitude, respectively. The second term on the RHS of Equation 3 has a different physical interpretation for compressible and incompressible flows, and only in the latter case can it directly provide information on the radial gradient of the radial flow, with $\frac{\partial u_r}{\partial r} = -\nabla_h \cdot \mathbf{u}_h - \frac{2u_r}{r}$.

In the case of a spherical rigid boundary at the top of the dynamo region, immediately below this boundary, $u_r = \frac{\partial u_r}{\partial \phi} = \frac{\partial u_r}{\partial \theta} = 0$. These conditions applied to Equation 3 lead to

$$\frac{\partial B_r}{\partial t} + (\mathbf{u}_h \cdot \nabla_h) B_r + B_r (\nabla_h \cdot \mathbf{u}_h) = 0 \tag{4}$$

Equation 4 is the common standard equation to invert for the flow at the top of the Earth's core. Note that it is valid for both compressible and incompressible flows, although, only for incompressible flow can we read the horizontal divergence directly as upwelling or downwelling below this boundary.

From Equation 4, only the horizontal distributions of the radial field and the horizontal flow contribute to the (poloidal) magnetic SV observed outside the dynamo region in case of a rigid boundary at the top of that region. However, assuming zero radial flow at the top of the dynamo region might not be valid for Jupiter, since the transition from molecular to metallic hydrogen is thought to be smooth. If this is the case, the three terms $(\mathbf{B}_h \cdot \nabla_h) u_r - u_r \frac{\partial B_r}{\partial r} - 2u_r \frac{B_r}{r}$ in Equation 3 should be retained. These terms depend on the horizontal magnetic field and the radial flow across the dynamo boundary as well as on the B_r at the boundary and the radial gradient of B_r below this boundary. However, our knowledge about the Jovian interior is incomplete. Analytical, numerical and experimental work on models of the Jovian interior using gravity data (e.g., Militzer & Hubbard, 2023) and experimental measurements (Brygoo et al., 2021) suggest a pressure-dependent immiscibility of helium and hydrogen and helium rain precipitation, a possible mechanism at the origin of a stably stratified layer (SSL) below the strong Jovian zonal winds (e.g., Moore et al., 2022; Wicht & Gastine, 2020; Wulff et al., 2022). The location of this SSL and its radial extent are strongly debated. Some studies place it at deeper depths, between 0.8 and 0.9 R_J (Debras & Chabrier, 2019) while other studies find a preferred depth between 0.9 and 0.95 R_J (Gastine & Wicht, 2021). Moreover, the depth at which the electrical conductivity steep transition occurs from very low to very high values is also debatable. Ab-initio calculations find this transition at about 0.9 R_J (French et al., 2012), while experimental results obtained in diamond-anvil cells suggest that the transition from metallic to molecular hydrogen occurs between 0.68 and 0.84 R_J (Brygoo et al., 2021). In this study we downward continue the MF and SV models to the depth level where we obtain our flow solutions, and use Equation 4 to compute a purely horizontal flow, as is commonly done for Earth and as was performed by Ridley and Holme (2016) for Jupiter. This approach is compatible with the existence of an SSL at a shallower location encompassing the transition from very low to very high electrical conductivity predicted by French et al. (2012) or, otherwise, with a deeper SSL encompassing the electrical conductivity transition proposed by Brygoo et al. (2021). Accordingly, and to take into account the current uncertainty in Jupiter internal models, we compute the flow at the different depths 0.8, 0.83 and 0.9 R_J.

3. MF and SV Models for Inversion

We use two input MF and SV models, Sharan et al. (2022a) and Sharan (2023) for our flow solutions. The two models are available up to spherical harmonic degrees 16 and 8 for the MF and SV, respectively (Figure 1). The model by Sharan et al. (2022a) was estimated using the Juno magnetic measurements acquired between August 2016 and July 2020, a total of 28 Juno orbits. The spherical harmonic coefficients of the field and SV were obtained by applying a weighted least squares inversion and the time variation was calculated using splines of order 2 with the knot spacing of about 1.95 years. The model by Sharan (2023) was estimated using the satellite data ranging from August 2016 to November 2021, a total of 38 orbits. While the methodology for both inversions remained basically the same, the knot spacing for the latter model increased to about 2.62 years. However, Juno orbits cover the northern hemisphere closer to the surface as compared to the southern hemisphere and this asymmetry gets more pronounced with time.

We denote the Sharan et al. (2022a) and Sharan (2023) models by SV28 (computed at epoch 2018.6) and SV38 (computed at epoch 2019.4), respectively, where 28 and 38 refer to the number of Juno perijoves used for each inversion. The resulting MF models provide very similar field features and as a result the inferred upper boundary of the dynamo convective region comes out at 0.830 ± 0.022 Jupiter radius for both models. Moreover, the SV timescales are also similar indicating that the field is dominated by advection. Nonetheless, some morphological differences can be detected between the two SV models, for example, the SV near the GBS is stronger in the model of Sharan et al. (2022a) and the SV near the south pole is stronger in the model of Sharan (2023). Since the two models were computed for two epochs with less than 1 year difference, that is likely much shorter than the advection time in Jupiter's interior, any flow differences we obtain will be interpreted as being mainly due to the different data sets. Although SV28 uses less data than SV38, the additional data in SV38 is biased due to more

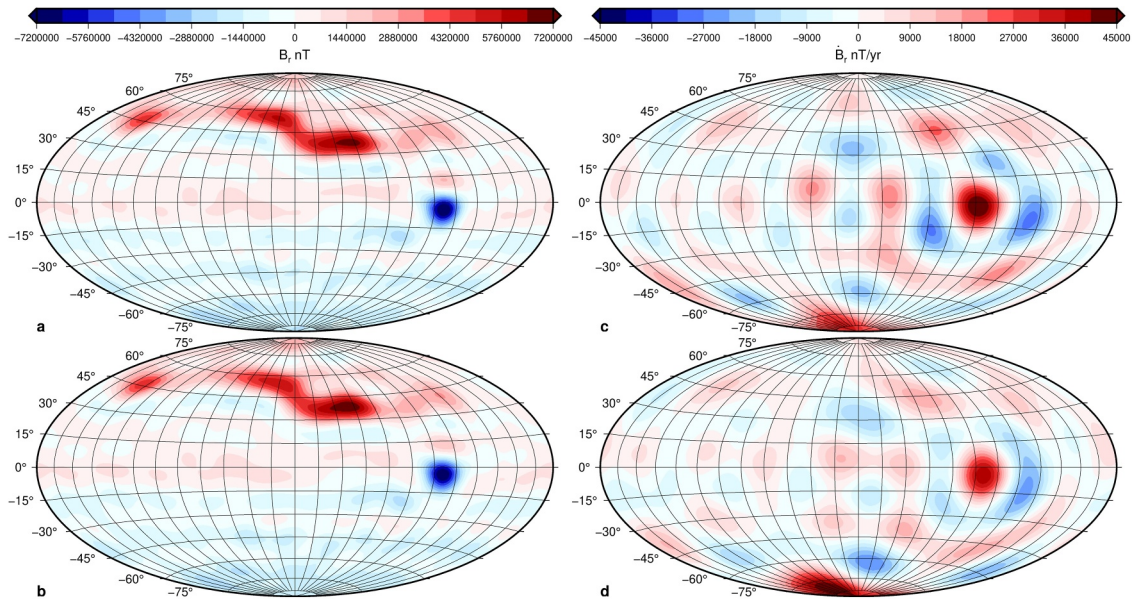

Figure 1. The radial MF in nanotesla (a, b) and its SV in nanotesla/year (c, d) using the models of Sharan et al. (2022a) (top) and Sharan (2023) (bottom) at Jupiter's dynamo radius (0.83 R_J). The maps are displayed using the Hammer projection with the latitude (y-axis) centered at the equator and longitude (x-axis) centered at 180° longitude in System III coordinate system, both in degrees, and with grid line spacing of 15°.

data coverage at lower altitudes in Jupiter's northern hemisphere compared to the southern region. We hence discuss the flow on top of Jupiter's dynamo region using both models, in order to determine the most robust features of the computed solutions.

4. Inversion for the Flow at the Top of the Jovian Dynamo

Equation 4 is the radial induction equation at the top of the dynamo region which is commonly used to invert the geomagnetic SV and MF models for the flow at the top of the Earth's core using various physical assumptions (Holme, 2015). We use the two models described in the previous section for Jupiter and invert this equation at a radius of 0.83 R_J, which is the estimated top of Jupiter's dynamo region according to analyses of the Jovian magnetic field energy spectrum (Sharan, 2023; Sharan et al., 2022a).

We invert SV28 and SV38 to derive snapshots of the flow up to spherical harmonic degree 16, since there is a sufficiently large number of MF and SV coefficients contributing to resolve the highest degree flow structures. To reduce the non-uniqueness inherent to the inverse problem, obtaining flow solutions requires additional physical assumptions (Bloxham & Jackson, 1991; Holme, 2015). Here we test three different assumptions that have been used in the context of flow at the top of Earth's outer core-purely toroidal (Whaler, 1980), tangential geostrophic (Le Mouël, 1984) and columnar flows (Amit & Olson, 2004). There is additionally a large-scale flow regularization, which we combine with the previous physical assumptions, or apply alone. These various assumptions are imposed using standard regularized least squares inversion (Pais et al., 2004, 2014; Pais & Jault, 2008). To test the sensitivity of our results to the assumed value of the dynamo radius, we also invert for the flow based on our field models downward projected to 0.8 R_J as well as 0.9 R_J which is the radius at which some Jovian numerical dynamo simulations place the dynamo outer boundary (e.g., Tsang & Jones, 2020; Wicht et al., 2019).

In spherical radial, co-latitude and longitude coordinates r, θ and ϕ, the radial magnetic field and its time derivative can be written as

$$B_r = \sum_{n=1}^{\infty} \sum_{m=0}^{n} (n+1)\left(\frac{a}{r}\right)^{n+2} \left[g_n^m \cos m\phi + h_n^m \sin m\phi\right] P_n^m(\cos\theta) \tag{5}$$

$$\frac{\partial B_r}{\partial t} = \sum_{n=1}^{\infty} \sum_{m=0}^{n} (n+1)\left(\frac{a}{r}\right)^{n+2} \left[\dot{g}_n^m \cos m\phi + \dot{h}_n^m \sin m\phi\right] P_n^m(\cos\theta) \tag{6}$$

where a is the radius of the planet, (g_n^m, h_n^m) and ($\dot{g}_n^m$, $\dot{h}_n^m$) are the MF and SV spherical harmonic Gauss coefficients defined at the planetary surface, n and m are spherical harmonic degree and order, respectively, and $P_n^m(\cos\theta)$ are the associated Schmidt semi-normalized Legendre functions. The Gauss coefficients from SV28 and SV38 models (Section 3) serve as input in the flow inversion. The tangential flow at the top of the dynamo region (radius R), where $u_r = 0$, can be written as

$$\mathbf{u}_h(\theta,\phi) = R\nabla_h \times (T\hat{\mathbf{r}}) + R\nabla_h P \tag{7}$$

where the toroidal (T) and poloidal (P) velocity scalar potentials are also expanded in terms of spherical harmonics as

$$T = R\sum_{n=1}^{\infty}\sum_{m=0}^{n}\left[t_n^{m,c}\cos m\phi + t_n^{m,s}\sin m\phi\right]P_n^m(\cos\theta) \tag{8}$$

$$P = R\sum_{n=1}^{\infty}\sum_{m=0}^{n}\left[p_n^{m,c}\cos m\phi + p_n^{m,s}\sin m\phi\right]P_n^m(\cos\theta) \tag{9}$$

The spherical harmonic coefficients in Equations 8 and 9 are determined in the flow inversion. Inserting Equations 5–9 into Equation 4, we obtain the linear matrix equation $\mathbf{Ax} = \mathbf{y}$ where $\mathbf{x}$ and $\mathbf{y}$ are vectors with spherical harmonic coefficients of the flow scalar functions (T and P) and the SV, respectively, and $\mathbf{A}$ represents the interaction or design matrix (e.g., Jackson & Finlay, 2007). We use regularized least squares to minimize the objective function

$$\Phi(\mathbf{x}) = (\mathbf{Ax}-\mathbf{y})^T\mathbf{C}_y^{-1}(\mathbf{Ax}-\mathbf{y}) + \sum_i \lambda_i \mathbf{x}^T\mathbf{C}_i^{-1}\mathbf{x} \tag{10}$$

where $\mathbf{C}_y$ represents the covariance matrix for the SV coefficients, $\mathbf{x}^T\mathbf{C}_i^{-1}\mathbf{x}$ are regularization terms representing different flow assumptions written in a quadratic form, and λ_i are damping parameters, tuned in order to impose the physical assumptions with different strengths. Solving for the linear equation $\mathbf{Ax} = \mathbf{y}$ under the above constraints provides the flow solution (e.g., Amit & Pais, 2013; Pais et al., 2004; Pais & Jault, 2008):

$$\mathbf{x} = \left(\mathbf{A}^T\mathbf{C}_y^{-1}\mathbf{A} + \sum_i \lambda_i\mathbf{C}_i^{-1}\right)\mathbf{A}^T\mathbf{C}_y^{-1}\mathbf{y} \tag{11}$$

Below we describe the SV covariance matrix and the physical assumptions used in this study.

4.1. SV Covariance Matrix ($\mathbf{C}_y$)

When inverting SV28 or SV38 for a flow solution, the goal is to explain the data by minimizing the misfit, but not to overfit the data because some unavoidable errors exist. Two kinds of errors arise from (a) imperfect magnetic field observations and assumptions in SV modeling ('data' error, 'd'), and (b) the induction of large-scale SV by interaction of unresolved small-scale field with the computed flow (modeling error, 'm') (Eymin & Hulot, 2005; Pais & Jault, 2008). The λ_i parameters must be such that the following condition holds

$$\chi = \sqrt{\frac{(\mathbf{Ax}-\mathbf{y})^T\mathbf{C}_y^{-1}(\mathbf{Ax}-\mathbf{y})}{N_y}} \sim 1 \tag{12}$$

where χ is the non-dimensional normalized misfit and N_y is the total number of SV coefficients. We consider $\mathbf{C}_y$ diagonal with degree-dependent components of the form $\sigma(n)^2 = \sigma^d(n)^2 + \sigma^m(n)^2$ (Amit & Pais, 2013; Gillet et al., 2009; Pais et al., 2014), where $\sigma^d(n)$ and $\sigma^m(n)$ represent the estimated uncertainties due to SV model computation and due to under-parameterization of the MF.

Table 1
Parameters for the Analytical Expression of the Modeling Error σ^m (n) (K and α in Equation 15) and Regularization Parameter λ_E That Multiplies the Large-Scale Flow Constraint for the Different Solutions

Flow model	K $(nT/yr)^2$	α	λ_E
L (modA)	1.37	0.094	5.25e+6
L (modB)	0.87	0.076	7.25e+6
T (modA)	19.01	0.016	1.50e+5
T (modB)	18.92	0.016	1.25e+5
TG (modA)	19.10	0.018	1.25e+5
TG (modB)	22.23	0.009	1.25e+5
CF (modA)	26.18	0.018	2.5e+4
CF (modB)	34.59	0.007	2.5e+4

For the uncertainty related to the SV coefficients, we use the error in each coefficient $\left(\Delta \dot{g}_n^m, \Delta \dot{h}_n^m\right)$ estimated during inversion of Juno data to obtain the SV model (Sharan, 2023; Sharan et al., 2022b). We calculate the SV spectra S_n associated with this error for each degree n

$$S_n = (n+1)\sum_{m=0}^{n}\left[\left(\Delta \dot{g}_n^m\right)^2 + \left(\Delta \dot{h}_n^m\right)^2\right] \tag{13}$$

and divide it by the number of coefficients corresponding to that degree to estimate an average data error variance per degree

$$\sigma^d(n)^2 = \frac{S_n}{(2n+1)(n+1)} \tag{14}$$

To account for the possible impact of the (unknown) small-scale MF on the large-scale SV, we first fit a straight line to the logarithm of the MF spectra from $n = 2$ to 16 and then use this linear model to extrapolate the field to degree 40. The coefficients extrapolated to beyond degree 16 are treated as Gaussian random quantities with zero mean and variance dependent only on the degree and not on the order, that is we assume statistical isotropy of the MF small scales. Using the linear regression parameters computed for SV28 and SV38, we calculate 20 random realizations of the small-scale Gauss coefficients of the magnetic field at each epoch.

We then invert for the flow in an iterative calculation, during which the parameter $\lambda_i = \lambda_E$ in Equation 11 that imposes the large scale flow constraint (see Section 4.2.1) is made to change. The calculation comprises two cycles at each step i (Pais et al., 2014):

- *Misfit-tuning cycle:* iterative search for the best regularization parameter λ_E for which the inverted flow explains the SV data within the errors by verifying the condition $1 - \epsilon < \chi < 1 + \epsilon$ (ϵ is a very small quantity).
- *Error-updating cycle:* computation of the advection of small-scale field (20 realizations) by the flow computed in the misfit-tuning cycle, in order to update the modeling error, which is then used in step i+1.

In this iterative multivariate inversion, an exponential law is fitted to the modeling error, as was the case in Pais and Jault (2008) and Amit and Pais (2013).

$$\sigma^m(n)^2 = Ke^{\alpha n} \tag{15}$$

where we compute parameters K and α for the different models and the different assumptions on the flow (Table 1). The final analytical expression for the diagonal components of $\mathbf{C}_y$ is the sum of the two variances (Equations 14 and 15) which is used in the misfit-tuning cycle.

The iterative approach stops when the inverted flow converges. Our computed flow hence explains the (large-scale) SV model as a result of advection of both the modeled large-scale field ($n \leq 16$) and the extrapolated small-scale field ($17 \leq n \leq 40$).

4.2. Flow Assumptions

In order to reduce the inherent non-uniqueness of the inverse problem solution, we need to introduce an additional equation which comes from assuming some specific behavior for the flow (Holme, 2015). The constraints we apply in this study have been commonly used for the Earth's outer core. Two of these assumptions rely on the dominance of rapid rotation effects, whereas a third one reflects the presence of an SSL at the top of the dynamo region. We consider these dynamical effects to likely prevail at Jupiter's interior as well and test the assumptions to invert for the flow at the top of the Jovian dynamo region. In the end, they are built in the inversion through the elements of matrices C_i (Equation 10) that impose specific relations between different flow coefficients. For the explicit form of C_i, see Pais et al. (2004, 2014) and Pais and Jault (2008).

Here we present the four constraints that we apply in order to obtain different flow solutions. The first case merely forces the flow to be large scale (L), whereas the other three constraints are motivated by different a priori regarding the flow dynamics: toroidal flow (T), tangentially geostrophic flow (TG) and incompressible columnar flow (CF). To enforce each of the three physical constraints T, TG and CF, we multiply a sufficiently high damping parameter λ_i by the corresponding quadratic form that needs to be canceled (see Equation 10). Above this chosen value, the flow solution is no longer sensitive to changes of λ_i (Pais et al., 2004). The constraint that penalizes small flow scales is multiplied by λ_E. A different λ_E is computed for each inversion, inside the iterative misfit-tuning cycle (see Section 4.1 and Table 1).

4.2.1. Large-Scale Flow (L)

We provide no a priori physical assumption for the flow and only apply a spatial regularization where we minimize the integral sum of squares of the horizontal divergence and radial vorticity $\left(\int_R \left[(\nabla_h \cdot \mathbf{u}_h)^2 + (\hat{r} \cdot \nabla_h \times \mathbf{u}_h)^2\right] dS\right)$ on the dynamo surface to obtain flows that are large scale (e.g., Gillet et al., 2009). The imposed normalization of the flow coefficients depends on the flow degree n as $(2n + 1)/[n(n + 1)]^2 \propto n^{-3}$. This large-scale assumption is also present for the three other flow solutions discussed below, though to a lesser extent (smaller damping parameter λ_E in Table 1).

4.2.2. Toroidal Flow (T)

Toroidal flow is based on the assumption that the motion is non divergent on the 2D spherical surface. In the case of an incompressible fluid, this means that no upwelling or downwelling occurs, for instance due to the presence of a stably stratified layer (Whaler, 1980). Hence

$$\nabla_h \cdot \mathbf{u}_h = 0 \tag{16}$$

and $P = 0$ in Equation 7.

4.2.3. Tangentially Geostrophic Flow (TG)

Tangential geostrophy relies on the assumption that the horizontal equilibrium of forces at the top of the dynamo region is dominated by the Coriolis and pressure gradient forces (Le Mouël, 1984). It can be represented as

$$\nabla_h \cdot \mathbf{u}_h = \frac{\tan\theta}{R} u_\theta \tag{17}$$

4.2.4. Columnar Flow (CF)

Columnar flow relies on the assumption that Coriolis and pressure gradient dominate the force balance inside the whole dynamo region. Consequently, according to the Taylor-Proudman theorem, the flow does not vary in the direction of the planetary axis of rotation z. One immediate consequence of this z-invariance is that the flow must be symmetric about the equator. However, this theorem cannot apply precisely in the presence of non-parallel and rigid boundaries as is the case for spherical shells that host dynamos in deep planetary interiors. The adjustment of cylindrical fluid columns (Busse, 1975) to these non-parallel boundaries gives the following relation for an incompressible flow (Amit & Olson, 2004; Pais & Jault, 2008)

$$\nabla_h \cdot \mathbf{u}_h = 2\frac{\tan\theta}{R} u_\theta \tag{18}$$

Note the similarity between Equations 17 and 18, both of which rely on the dominance of rapid rotation effects (for more details see Amit & Pais, 2013).

Table 2
RMS of the SVa priori and Prediction Errors ($\langle\sigma\rangle$ and $\langle e\rangle$ in nT/yr) and RMS for the Full Velocity ($\langle v\rangle$ in km/yr), as Well as the Ratio of RMS Velocities of Equatorially Antisymmetric (A) to Equatorially Symmetric (S), Poloidal (P) to Toroidal (T) and Non-zonal (NZ) to Zonal (Z) Components for the Different Models at the Dynamo Radius 0.83 R_J

Flow model	$\langle\sigma\rangle$	$\langle e\rangle$	$\langle v\rangle$	$\langle v\rangle_A/\langle v\rangle_S$	$\langle v\rangle_P/\langle v\rangle_T$	$\langle v\rangle_{NZ}/\langle v\rangle_Z$	$\langle v\rangle_{0.8}$	$\langle v\rangle_{0.9}$
L (SV28)	125.6	128.0	143.2	0.46	0.66	0.72	138.7	126.6
L (SV38)	194.6	201.5	98.0	0.43	0.66	0.61	97.0	88.4
T (SV28)	512.6	575.0	299.6	0.69	0	1.00	238.3	543.2
T (SV38)	533.8	565.6	274.2	0.88	0	1.65	198.0	568.5
TG (SV28)	521.9	552.6	306.2	0.64	0.19	1.29	244.5	557.2
TG (SV38)	592.6	663.1	253.4	0.88	0.12	1.99	189.8	548.5
CF (SV28)	708.0	645.2	393.0	0	0.33	2.05	271.1	643.1
CF (SV38)	881.3	894.5	337.0	0	0.22	1.86	246.0	638.6

Note. The full velocity RMS is also displayed for the inversions with field and SV models at dynamo radii of 0.8 and 0.9 R_J. The RMS SV for SV28 and SV38 at 1 R_J are 2,859.3 nT/yr and 2,578.3 nT/yr respectively. All RMS values are computed according to Equations 19 and 20.

5. Results

5.1. Global Flow Features

We now describe the results obtained for all four flow solutions. Table 2 displays the root mean square (RMS) error $\langle e\rangle$ as well as the RMS velocity $\langle v\rangle$ for the total velocity, the equatorially symmetric (S) and antisymmetric (A), toroidal (T) and poloidal (P), and zonal (Z) and non-zonal (NZ) components. RMS values for the SV prediction error and for the flow amplitude are computed over a spherical surface S with the radius R of the top of Jupiter's dynamo region:

$$\langle e\rangle = \left[\frac{1}{4\pi R_J^2}\int_S \left(\dot{\mathbf{B}}^{mod} - \dot{\mathbf{B}}^{pre}\right)\cdot\left(\dot{\mathbf{B}}^{mod} - \dot{\mathbf{B}}^{pre}\right) dS\right]^{1/2} \tag{19}$$

$$\langle v\rangle = \left[\frac{1}{4\pi R^2}\int_S \mathbf{v}\cdot\mathbf{v}\, dS\right]^{1/2} \tag{20}$$

where, $\dot{\mathbf{B}}^{mod}$ is the input SV (from SV28 or SV38 model) and, $\dot{\mathbf{B}}^{pre}$ is the predicted SV, obtained from inserting the flow solutions into the radial induction equation (Equation 4). The lowest error $\langle e\rangle$ is observed for the L flow because it has the smallest sub-grid contribution, σ^m: a large-scale flow generates almost no large-scale SV when interacting with small scales of the MF, and the misfit level is determined by σ^d (Note that the a priori SV errors associated with the different flow models are also different, and SV estimates are allowed to deviate from the SV model accordingly). Moreover, this flow is not constrained by any physical assumption and hence requires a large damping coefficient (λ_E in Table 1) which attenuates small scale flows in a non-realistic way leading to the lowest values for the flow velocity. The RMS velocity for the flow over S at the top of the dynamo region is also displayed. The L flow has the lowest kinetic energy as expected, the T and TG flows show comparable magnitudes and the CF flow displays the largest velocity magnitudes. One possible explanation is an increase of the contribution of "invisible" flows in the case of the CF solution, that is, flows that do not generate SV. This increase can be due to an increase in the size of ambiguous regions (regions on the boundary of the dynamo region that are delimited by particular contours that do not cross the equator; Amit and Pais (2013)). Otherwise, it can be due to the increase in the intensity of flows inside the ambiguous regions as a way to verify the imposed equatorial symmetry constraint. 'Invisible' flows are present in T and TG flows, where they can be found circulating around iso-contours of B_r (T flow) or iso-contours of $B_r/\cos\theta$ (TG flow). In all three cases, we will further discuss about "invisible" flows contribution to our solution, referring them as "field-aligned" flows (Finlay & Amit, 2011). For all cases, the velocities are larger for SV28 than SV38, as required by the stronger SV at low latitudes in the former (Figure 1). All models show a stronger symmetric component (flow is perfectly symmetric by construction for CF). However, somewhat surprisingly, the anti-symmetric component is far from being negligible in L, T or

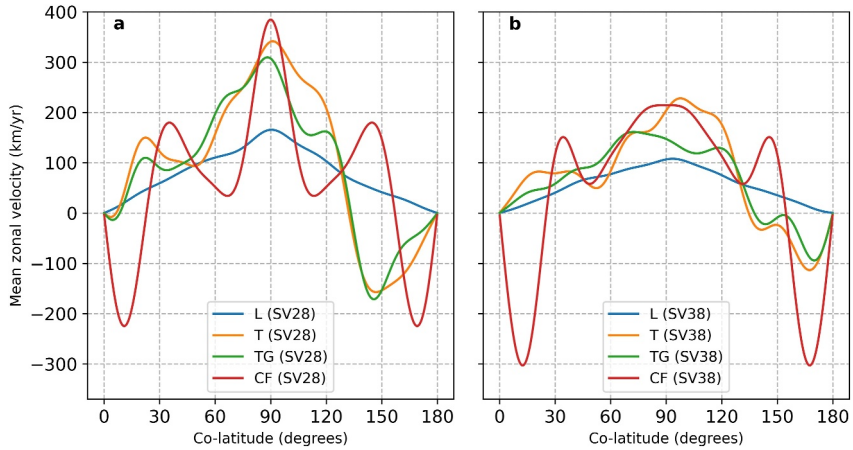

Figure 2. Zonal azimuthal velocity versus co-latitude for the large-scale (L), toroidal (T), tangentially geostrophic (TG) and columnar (CF) flows at the dynamo radius 0.83 R_J from inversion of (a) SV28 and (b) SV38.

TG flows, and in some cases it almost matches the symmetric component (e.g., T and TG in SV38). We recall that for the Earth's core, during the satellite era, inverted flows are strongly symmetric with respect to the equatorial plane (twice the antisymmetric components) (Finlay et al., 2010). The poloidal component is suppressed by construction in T flow, it is relatively weak in TG and CF cases, and rises to more than half the toroidal component for L flow. The poloidal flow in CF is about twice larger than in TG flow, as expected from the factor 2 difference between Equations 17 and 18. The zonal component is relatively stronger for the L flow, as expected for a large-scale flow (more zonal relative to non-zonal coefficients), but it is significantly weaker than the non-zonal components for most other cases (see in particular the CF flow).

We test the sensitivity of our results to the assumed depth of the dynamo region by further inverting the radial field and its SV at dynamo radii of 0.8 and 0.9 R_J. We note that $\langle v \rangle_{0.9}$ is about twice larger than $\langle v \rangle$ (which is computed at 0.83 R_J) for the T, TG and CF cases, while for the L flow there is a slight decrease. Conversely, for 0.8 R_J, the velocity for the T, TG and CF cases are lower while the values are very close for the L case. In general, higher truncation degrees in the MF than in the SV lead to a more pronounced increase in the power of MF than SV due to downward continuation. This is compensated by a decrease in the velocity when going from 0.9 R_J to 0.8 R_J (see Equation 4). The nearly practical independence of L flow $\langle v \rangle$ with depth means that the SV signal we are modeling (up to degree 8) is explained, in this case, by the large scale flow interacting with only the first degrees of the MF. Therefore, when downward continuing the MF and SV, the significantly higher energy at smaller scales (higher degrees) of the MF does not make a significant difference in $\langle v \rangle$. For different dynamo radii, the dependence on the physical assumption is preserved, that is, at all radii the L flows are the weakest, the CF flows are the strongest and T and TG flows show similar, intermediate, RMS velocity values.

Figure 2 displays the azimuthal velocities averaged over longitude (zonal flows) versus co-latitude. For all our solutions, the peak zonal flow appears near the equator pointing eastward except for the CF flow of SV38 that exhibits peak westward zonal flow at high latitudes. Furthermore, the solutions display a decreasing trend from the equator to the poles, monotonic in the case of L flow, oscillatory in the other cases. This trend, which is also present in Bloxham et al. (2022, 2024) using different approaches, is a consequence of the strong SV of the GBS. We also observe eastward zonal velocities at mid latitudes for all cases. At high latitudes, we find westward zonal flow for CF at both hemispheres, and for T and TG in the southern hemisphere, in agreement with thermal wind theory (Lézin et al., 2023). SV38 displays lower eastward zonal velocities near the equator compared to SV28 in all cases and larger westward velocities near the poles for the CF case. Note the striking agreement between the zonal velocity profiles of the T and TG flows, despite the different assumptions applied in the inversion of these two flow solutions.

Figure 3 displays the MF advection $(-\mathbf{u}_h \cdot \nabla_h B_r)$ and deformation $(-B_r(\nabla_h \cdot \mathbf{u}_h))$ (see Equation 4) due to the four flow models inverted from SV28 and SV38. Note that only for incompressible flows can the deformation term be readily identified with stretching/contraction of the field lines by upwelling/downwelling. The advection contribution to SV around the GBS is overwhelmingly dominant in all cases. Deformation is zero for T flow, by

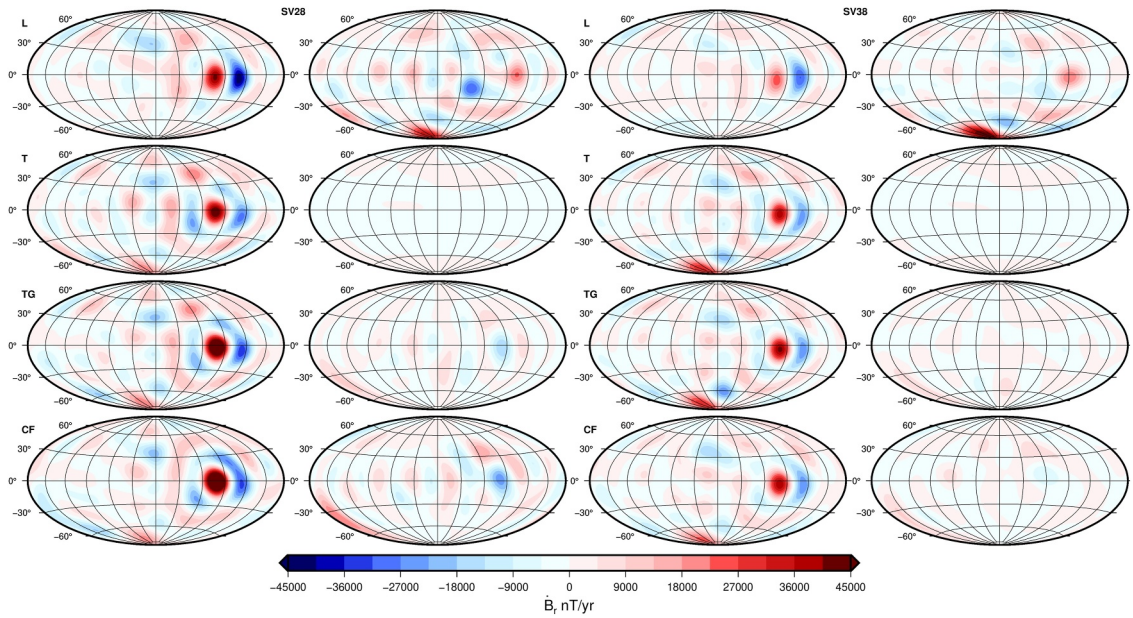

Figure 3. Advection (columns 1 and 3) and deformation (columns 2 and 4) contributions to the SV by the large-scale (L), toroidal (T), tangentially geostrophic (TG) and columnar (CF) flows using SV28 (columns 1 and 2) and SV38 (columns 3 and 4) at the dynamo radius 0.83 R_J. The maps are displayed using the Hammer projection with the latitude (y-axis) centered at the equator and longitude (x-axis) centered at 180° longitude, both in degrees, and with grid line spacing of 30°.

construction. The L flow shows a striking difference from the other flows near the south pole, where positive horizontal divergence suggesting local fluid upwelling disperses the magnetic field lines hence weakening the radial magnetic field. The TG and CF cases differ by a factor ∼2 in the horizontal divergence and consequently in the deformation effect (see Equations 17 and 18). Nevertheless, even in CF flow, deformation remains very weak compared to advection. The flows inverted from SV38 exhibit relatively stronger advective SV in the south pole and relatively weaker advective SV near the GBS compared to SV28, in agreement with the corresponding observed SV patterns (Figures 1c and 1d).

The detailed flow maps for all cases are shown in Figure 4. Overall, flow solutions from SV28 and SV38 display similar patterns, with higher intensities and in most cases smaller misfit errors (see Table 2) for SV28. The L flow displays a smooth pattern of dominant eastward azimuthal flow. The T and TG flow models have several common features, most notably eastward jets at low latitudes and vortices at high latitudes of the southern hemisphere. The CF flow is different because of its imposed equatorial symmetry. Nevertheless, the CF model shares some features with the T and TG models, including the dominant eastward flow near the equator (stronger for longitudes $0° < \phi < 180°$) and the southern high-latitude vortices. Obviously these vortices are mirrored to the northern high latitudes for the symmetric case CF, whereas in cases T and TG the northern hemisphere is characterized by dominant azimuthal and field-aligned flows.

We also obtain the global maps for the flow solutions at depths of 0.8 and 0.9 R_J dynamo radii. While the flow amplitudes differ (Table 2), the flow pattern at both these depths remains the same as at 0.83 R_J (Figure 4) for all four cases using both SV28 and SV38 models.

5.2. Regional Flow Features

Figure 5 displays zoom-ins to the flows in the region of the GBS (the prominent magnetic flux patch of negative polarity near the equator), superimposed on the field observed there (Figures 1a and 1b). All flow models exhibit eastward flow in this region, advecting the MF (Figure 3) corresponding to eastward displacement of the GBS. Indeed, the SV in this region is positive/negative, westward/eastward from the GBS, respectively (Figures 1c and 1d), indicative of eastward advection of a negative radial field feature (Amit, 2014). Neither TG nor CF flows can cross the equator. A major difference observed between these two cases can be seen north and south of the GBS where the CF solution displays strong westward flow (especially for SV28).

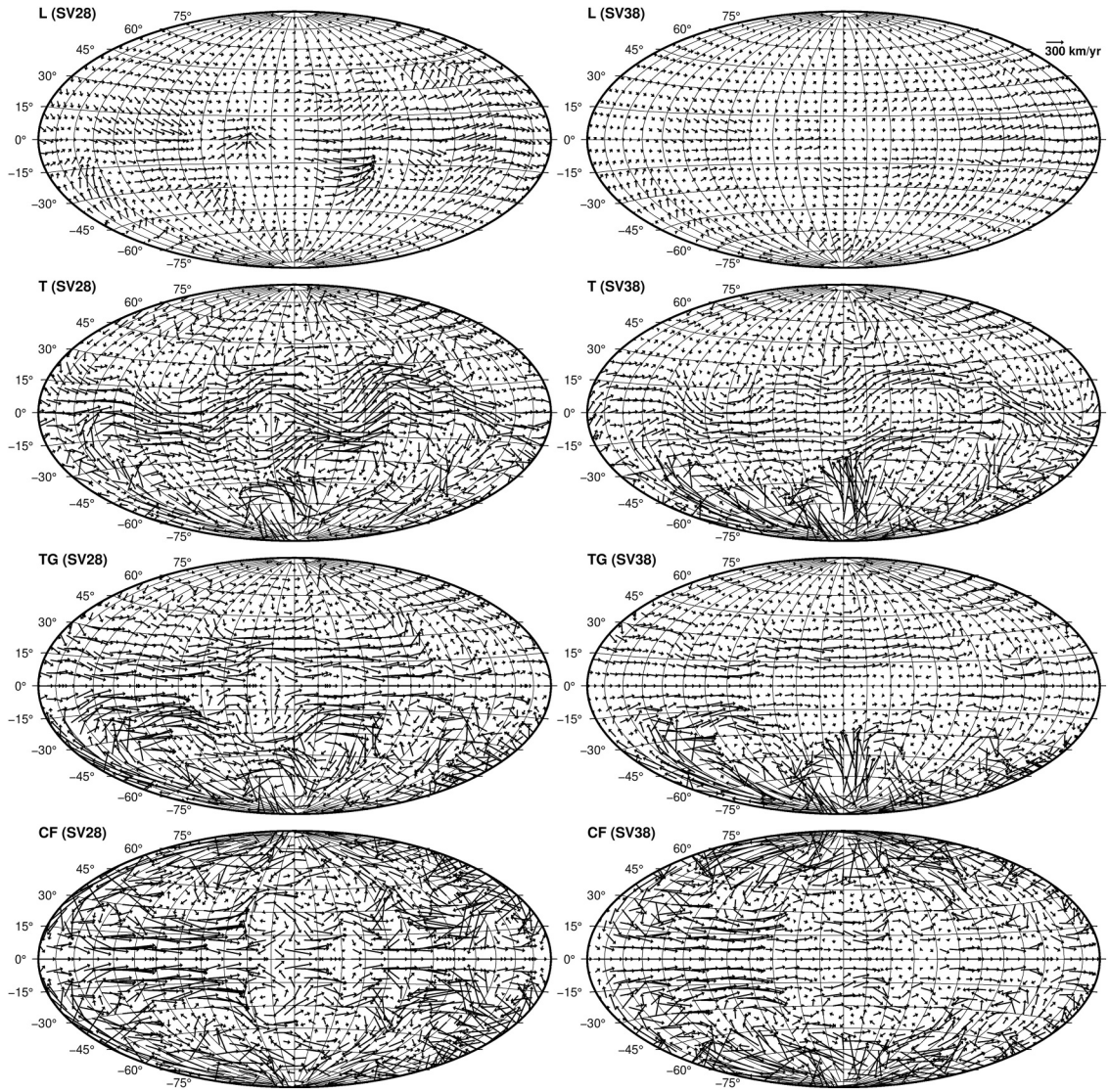

Figure 4. Global flow models obtained using the large-scale (L), toroidal (T), tangentially geostrophic (TG) and columnar (CF) assumptions at the dynamo radius 0.83 R_J for both SV28 and SV38 models. The maps are displayed using the Hammer projection with the latitude (y-axis) centered at the equator and longitude (x-axis) centered at 180° longitude, both in degrees, and with grid line spacing of 15°.

Figure 6 displays the polar southern hemisphere view of the flows superimposed on the observed MF. The opposite signs in the MF and the SV in the south pole region (Figure 1) is suggestive of local magnetic field dispersion by deformation due to flow upwelling in the case of incompressible flows (Amit, 2014). In case L, indeed, deformation of the radial magnetic field contours near the south pole is an efficient process to explain the SV there (see Figure 3). Nonetheless, the similarity among the T, TG and CF cases hints at an explanation for local SV that might not be related to deformation of the MF, but instead to advection of B_r. This mechanism requires a significantly larger complexity of the flow, as shown in Figure 6. The velocity observed at the south pole region for all cases is stronger for SV38, as required to explain a stronger SV signal there.

Figure 7 displays the zoom-ins to the flow at the region near the large positive magnetic flux patch at mid latitudes of the northern hemisphere. All cases show evidence of eastward flows. Note that the flow patterns are quite aligned with the contours of radial field, that is, induction efficiency is low in this region (Finlay & Amit, 2011). Although flows circulating along B_r contours are "invisible" only in the case of T flow, at these relatively high latitudes B_r contours are very close to contours that render "invisible" also TG and CF flows.

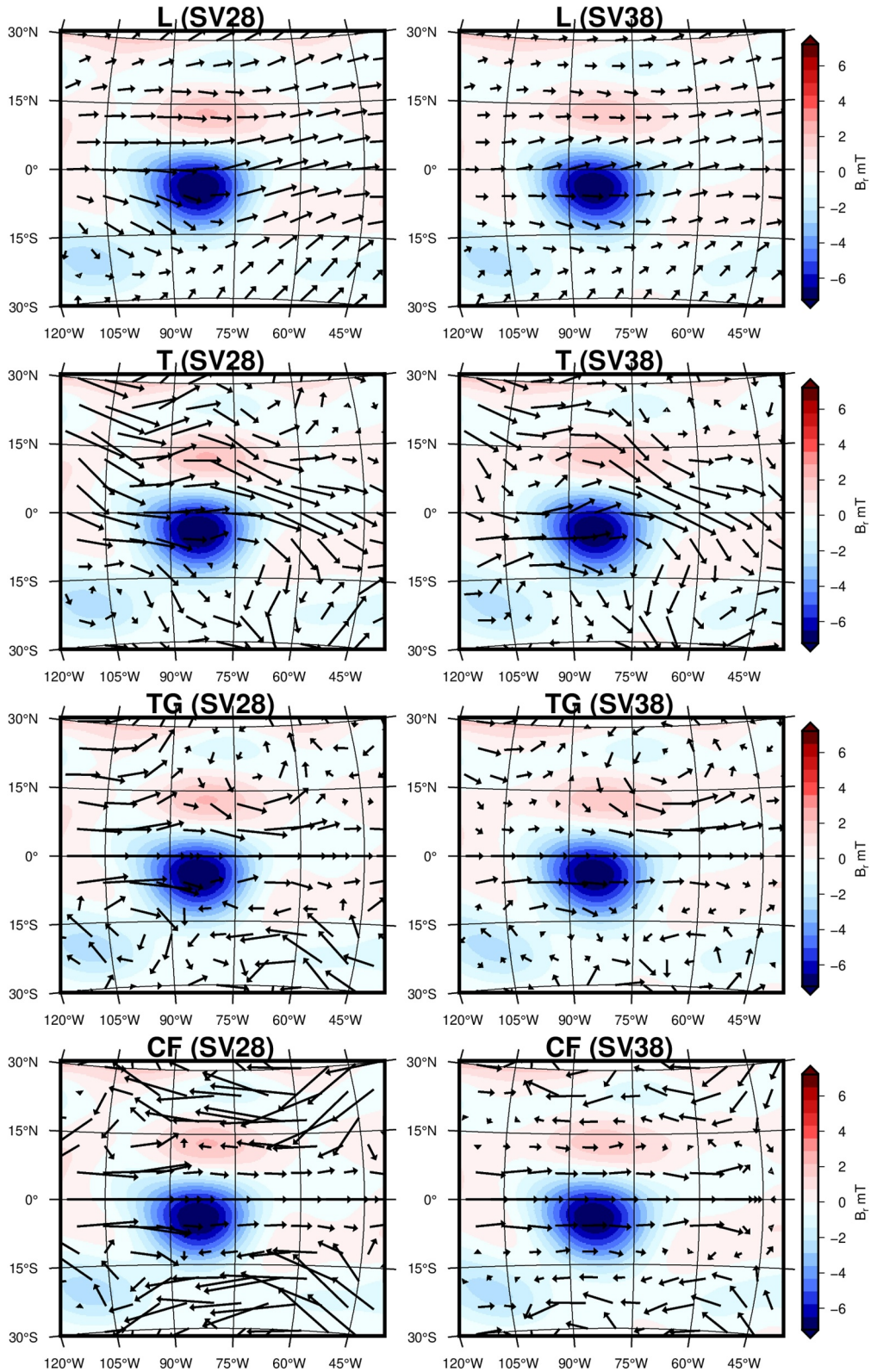

Figure 5. Zoom-in to the flow in the region of the Great Blue Spot for the large scale (L), toroidal (T), tangentially geostrophic (TG) and columnar (CF) flow solutions, superimposed on the radial field at the dynamo radius 0.83 R_J, for both SV28 and SV38 field models. The maps are displayed using the Lambert Azimuthal Equal-Area projection with the latitude (*y*-axis) and longitude (*x*-axis) in degrees.

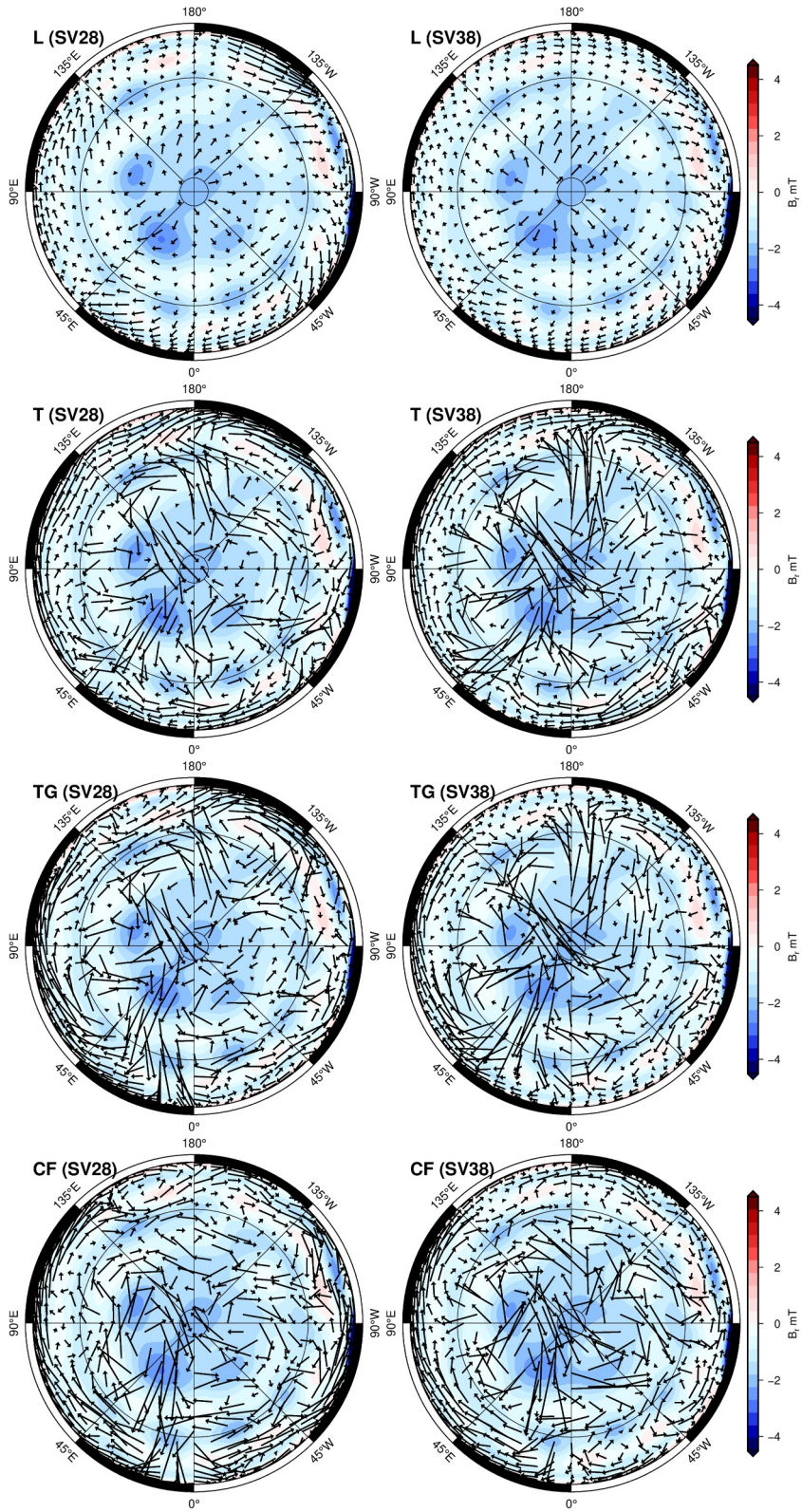

Figure 6. As in Figure 5 but for the south polar view using Orthographic projection. The latitude grid line spacing is 45°.

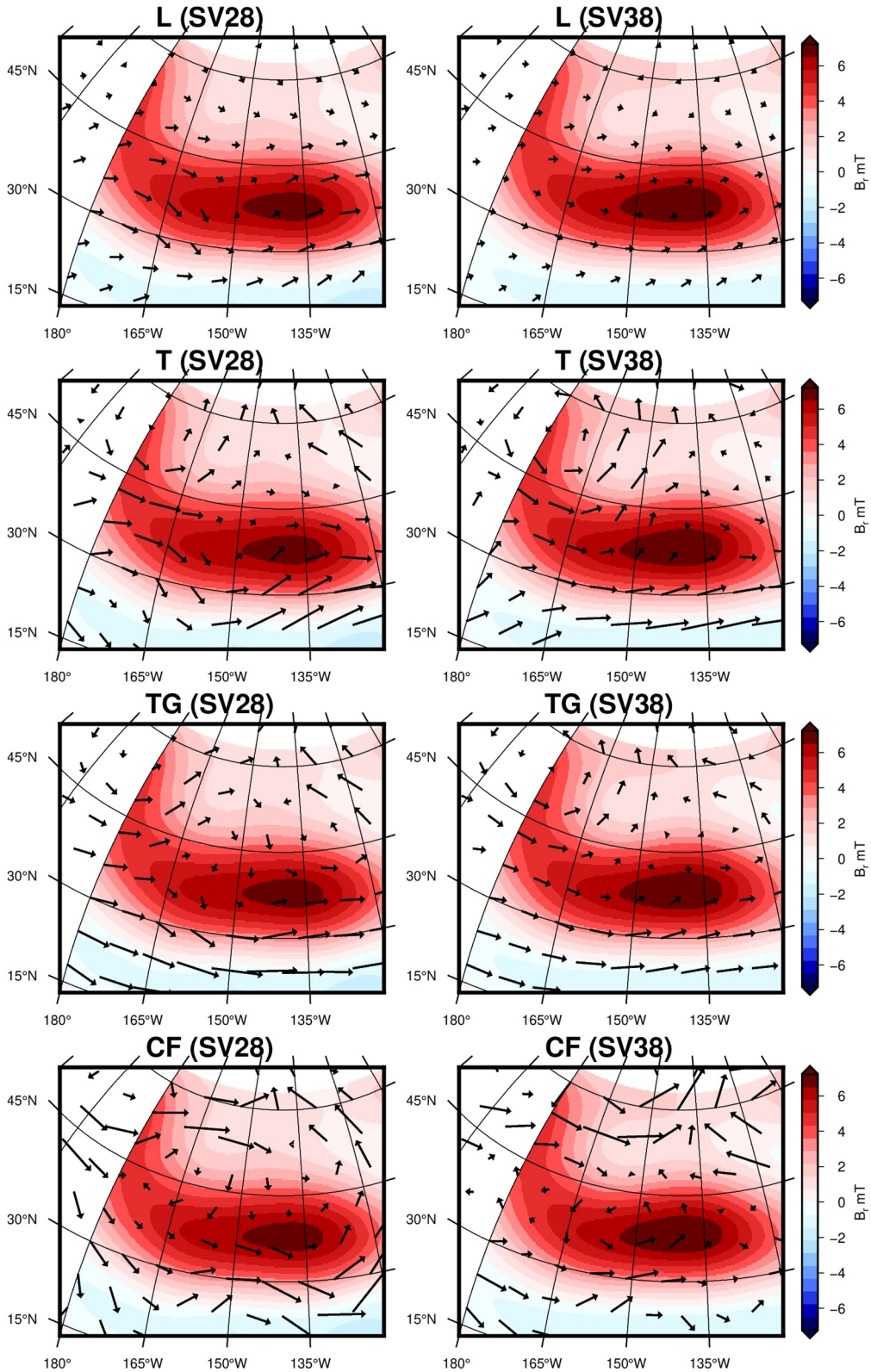

Figure 7. As in Figure 5 but for the large positive magnetic flux patch at mid latitudes of the northern hemisphere.

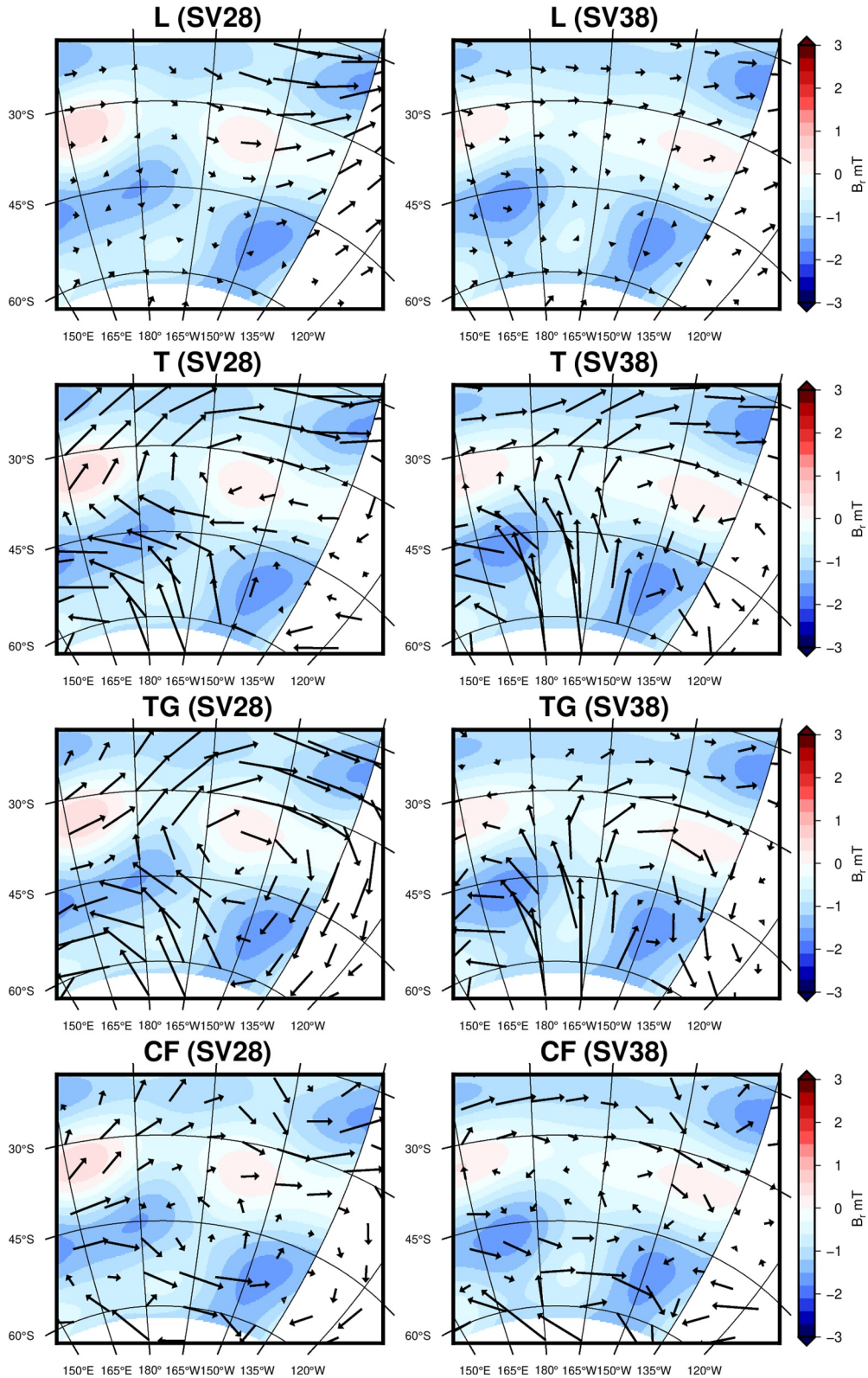

Figure 8. As in Figure 5 but for mid latitudes of the southern hemisphere.

Finally, Figure 8 displays the zoom-ins to the flow at the region of mid latitudes of the southern hemisphere where important deviations to purely azimuthal flows are observed (see Figure 4). The T and TG cases exhibit strong northward (i.e., equatorward) flows. Such meridional flows are absent in the large-scale L case because they are confined in space as well as in the CF case possibly due to constraints imposed by the SV features at mid latitudes of the northern hemisphere.

6. Discussion

We use four different assumptions to solve for the flow at the top of Jupiter's dynamo region-that the flow is large scale (L), purely toroidal (T), tangentially geostrophic (TG) or z-invariant and incompressible (CF). We find RMS velocities of the order of ∼100–400 km/yr (0.3–1.3 cm/s) at 0.83 R_J dynamo boundary (Table 2). The flows are obtained using two different field models, SV28 and SV38. While the two field models show very similar features, the global RMS SV is about 10% larger in SV28 than SV38 (Table 2). Locally, the SV is strongest near the GBS in SV28 model and largest at the South Pole in the case of SV38 (Figures 1c and 1d). Consequently, the fluid RMS velocities are larger for SV28 for all flow cases (Table 2), and the local differences between SV28 and SV38 reflect into stronger zonal flows at the equator from the first model (Figures 2 and 5) and stronger latitudinal flows close to the South Pole from the latter (Figure 6). The prediction errors are larger for flows computed from SV38 (Table 2) due to larger a priori errors ($\sigma^d(n)$, see Equation 14) in the model coefficients.

As expected from the SV maps (Figures 1c and 1d), we find evidence in the computed flow models for rich dynamical behavior in the Jovian interior. In fact, at different regions of the dynamo outer boundary, in addition to the dominant azimuthal eastward flow near the equator, the inverted flows show a variety of features including possible upwelling, unconstrained motion along B_r contours as well as meridional motion. These particular features are not very sensitive to the a priori concerning the flow dynamics (T, TG or CF) or the depth of the dynamo external boundary. Additionally, in all our flow models the SV is dominantly due to advection rather than deformation of the field (Figure 3). Maximum advection is observed for the GBS, especially for flows derived from SV28. Only the L case shows significant deformation effects, particularly for explaining the SV near the south pole.

A more quantitative analysis of our flow solutions (Table 2) shows that the RMS velocity of equatorial symmetric components $\langle v\rangle_{\mathrm{S}}$ are dominant for all flows, although the antisymmetric RMS velocity $\langle v\rangle_{\mathrm{A}}$ increases up to ∼90% of the symmetric counterpart for T and TG flows derived from SV38. This deviation in relation to equatorial symmetry is much stronger than what is observed for the Earth during the satellite era (e.g., Finlay et al., 2010) with values ∼50%. The T and TG flows essentially constrain the poloidal flow and hence are free to exhibit antisymmetry. The perfect equatorial symmetry in CF is imposed, and we report larger prediction errors in that case. As for the larger equatorial symmetry in the L case, it is consistent with results from dynamo simulations for the Earth where deviations from equatorial symmetry tend to increase for smaller scales, which are damped in L flows. This is due to a larger effect of magnetic compared to Coriolis forces for smaller scales, as measured by the Lehnert number (Gillet et al., 2011; Schaeffer et al., 2017). All the three tested physical assumptions, T, TG and CF solutions, imply a dominance of $\langle v\rangle_{\mathrm{T}}$ over $\langle v\rangle_{\mathrm{P}}$. However, when poloidal and toroidal coefficients are computed independently from each other, the RMS velocity of the poloidal component amounts to more than 60% of the toroidal RMS value, as is the case for flow L. An important feature contributing to explaining this result is the divergent flow at high latitudes in the southern hemisphere (Figure 3). As to zonal versus non-zonal features, all T, TG and CF flow solutions display a dominant non-zonal RMS velocity, as clearly stands out from flow vector charts (Figure 4) and can be confirmed through quantitative values (Table 2). Differently, in the case of the L flow solution, the strong imposed large-scale constraint explains the observed dominance of the zonal flow over the non-zonal part (Table 2).

We zoom-in the flows at locations where distinctive features of Jupiter SV have been pointed out before (Sharan et al., 2022a). All solutions display an intense eastward flow at the region of the GBS (Figure 5) which, as we further show, contributes only slightly to deform the GBS (Figure 3). Instead, the very strong SV feature observed at this region is mostly due to advection, for all flow solutions. A closer analysis shows that the CF flow exhibits westward jets above and below this prominent magnetic flux patch. These flows may lie in the ambiguous patches of the CF flow, in which case they are not constrained by the input models. Compared to the CF flow, the SV estimation errors are lower for the TG and T flows around the GBS for which flows tend to become eastward northern of the GBS, and be more meridional southern of GBS (Table 2 and Figure 9). This confirms that a

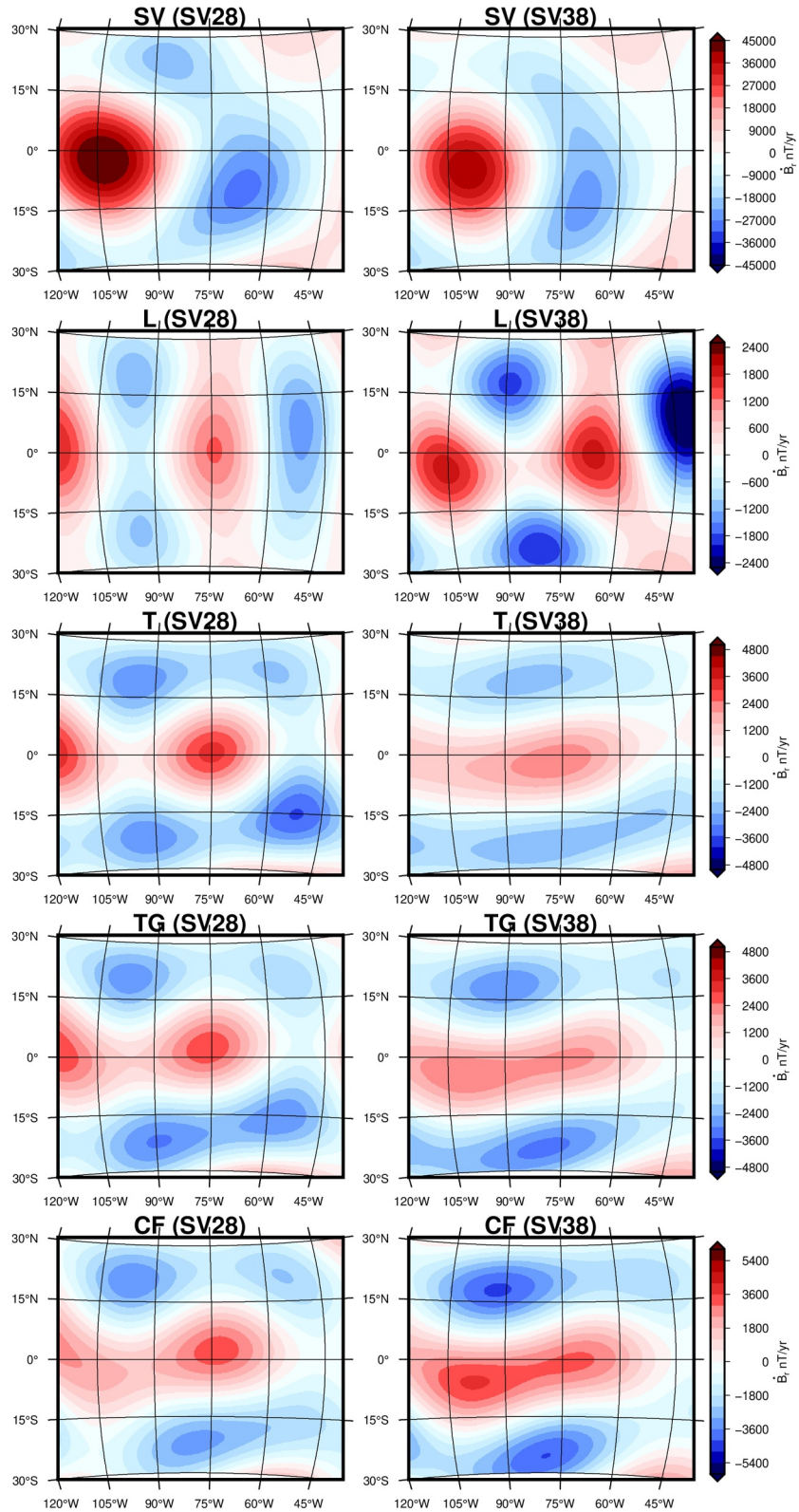

Figure 9. Zoom-in to the SV from SV28 and SV38 models (top row) and the difference between the input and predicted SV at the dynamo radius 0.83 R_J in the region of the Great Blue Spot for the large scale (L), toroidal (T), tangentially geostrophic (TG) and columnar (CF) flow solutions. The maps are displayed using the Lambert Azimuthal Equal-Area projection with the latitude (*y*-axis) and longitude (*x*-axis) in degrees. Note the difference in scales among the four flow solutions.

westward azimuthal current above and below the GBS is not required by the SV model. Furthermore and more generally, it brings attention to other possible biases in the CF model due to the associated strong assumptions applied to obtain the flow. This effect can also be noticed through the lower values of λ_E for this flow solution (Table 1), a sign that the smoothness (or large scale) condition is more difficult to impose on CF than on TG and T flows.

In the northern hemisphere, our L, T and TG models are dominated by large-scale zonal (eastward) flows (Figures 4 and 7). The CF model, however, maps the stronger complexity found in the southern hemisphere onto the northern hemisphere. All models display some field-aligned flows circulating around the large positive magnetic flux patch at mid latitudes (Figure 7). The 'invisibility' of these flows may explain the weak SV signal in the northern hemisphere at latitudes $\sim 30°$, in spite of relatively strong flow velocities close to the positive magnetic flux patch, especially in the case of T, TG and CF flows (Figures 1 and 4).

In the southern hemisphere we find significant meridional flows that cross an extended range of latitudes (Figure 4), preventing any clear signature of a tangent cylinder (the imaginary cylinder with its axis parallel to the rotation axis and its sides tangent to the inner solid core at the equatorial plane). At mid and high latitudes ($\leq -30°$) all T, TG and CF solutions reveal high intensity and complex flow features, including significant meridional (especially T and TG) and non-zonal flows (Figures 4, 6 and 8). Our MF and SV models display opposite signs at the south pole (Figure 1) which is suggestive of local fluid upwelling (Amit, 2014). However, this poloidal flow feature appears clearly only in the L case. Nevertheless, all our models exhibit westward jets at southern high latitudes (Figure 2). According to the thermal wind balance, vertical shear of the azimuthal flow is proportional to the meridional gradient of temperature (e.g., Lézin et al., 2023; Olson & Aurnou, 1999). Although we do not have direct access to the thermal distribution at Jupiter's interior, these high-latitude southern hemisphere westward flows are consistent with warm fluid rising at the south pole, a fluid upwelling that disperses magnetic field lines as manifested by the local opposite SV sign. The striking hemispherical contrast shown by all our solutions is suggestive of more vigorous convection in the southern hemisphere, which we speculate may be related to partial stratification. In the context of the Earth's core, it has been argued that such partial stratification may arise due to core-mantle boundary heat flux heterogeneity (Mound et al., 2019; Olson et al., 2017; Terra-Nova & Amit, 2024). The existence and origin of partial stratification at the top of the dynamo region of Jupiter is unknown. Nevertheless, our flow solutions may point to a magnetic signature of stronger stratification in the northern than in the southern hemispheres.

The zonal part of our solutions can be compared with previous studies focusing on purely zonal flows. We find latitude-dependent zonal values ranging between around -300 and $+400$ km/yr, at 0.83 R_J (Figure 2). The maximum zonal velocity from SV28 is eastward and localized at the equatorial region for all four flows. For SV38, the L, T and TG cases display peak eastward zonal velocity near the equator while the CF case displays peak westward zonal flow near the polar regions. Previous studies on Jupiter's internal flow estimation from magnetic field models focused on purely zonal flows. In Bloxham et al. (2022), the peak velocity of the localized equatorial jet in the GBS region is $\sim$270 km/yr at 0.9 R_J. Connerney et al. (2022) compared two different magnetic field models to suggest fluid velocity of $\sim$1,260 km/yr in the interior at 0.95 R_J. Using deep atmospheric zonal wind profiles to account for the SV, Moore et al. (2019) found a good fit assuming a magnetic drift velocity of $\sim$1,182 km/yr at 0.95 R_J. Their velocity reduces for lower depths. However, such fast zonal winds are not compatible with Jupiter's highly non-axisymmetric magnetic field at the surface (Wicht & Christensen, 2024). Our values are much lower, and we find increasing flow magnitude at a shallower depth (Table 2), a consequence of a stronger decrease in the MF than in the SV models farther from their region of generation, as a result of higher truncation degrees in MF than in SV and the more pronounced loss of power at the smaller scales. In addition, in Moore et al. (2019) the peak value is in the northern hemisphere near 10° latitude. They also suggested shear of the GBS due to the zonal winds, which we find no evidence of. The zonal flows from our solutions, required to explain Jupiter's magnetic field changes caused by azimuthal advection, are much weaker than Jupiter's atmospheric zonal jets, but comparable to previous estimates using magnetic field models (Bloxham et al., 2022, 2024). However, differently from the above mentioned studies, our flows also include significant meridional and non-zonal contributions.

Compared to the jets that are observed in the atmosphere of Jupiter, the velocity at the interior is expected to be much weaker (e.g., Porco et al., 2003; Simon-Miller & Gierasch, 2010). From the zonal wind profile of Simon et al. (2015), a maximum velocity of about $\sim 4.8 \times 10^6$ km/yr is observed at 24°N latitude. The profile displays

relatively low velocity right at the equator but with increasing values on either side of it for about 10° latitudes. However, these jets are strongly damped before depths of about 0.95 R_J (Christensen & Wulff, 2024; Gastine & Wicht, 2021; Kaspi et al., 2018). We therefore speculate that the zonal winds in Jupiter's atmosphere do not play a significant role in the SV generation, at the radial levels of 0.83 or 0.90 R_J where we compute our flows. In addition, our analysis does not allow to discriminate between flow advection and waves as causing the SV, due to the short covered period. This contrasts with Bloxham et al. (2024) who used more than 4 years of data.

Our flow solutions admit meridional and non-zonal contributions, as in Ridley and Holme (2016). Ridley and Holme (2016) found similar dominant flow near the equator using an inversion for a (degree 7) flow solution with their MF and SV models (JSV model) up to degree 7. However, they had confidence in their SV model only until degree 2, and there was little power in their small-scale SV model. Our results are hence more robust, since our parameterization of magnetic field and flow models allows to include significantly smaller scales, which we argue are well-constrained by the used data sets. In addition, while the inversion technique and regularization of Ridley and Holme (2016) are similar to ours, they did not account explicitly for sub-grid effects. Their study suggests velocities of $\sim$ 200 km/yr at 0.85 R_J, flow similarities between the toroidal and tangentially geostrophic cases for high damping levels, and some symmetry about the equator, all in qualitative agreement with our results. They find their results to be consistent with cylinders aligned with the rotation axis, suggestive of Busse columns typical to rapidly rotating systems. CF flows in our study also show the imprint of possible z-invariant columns reaching the dynamo boundary at latitudes above $\pm 15°$ (Figure 4).

The largest RMS SV errors for all flow solutions are observed for the southern pole region (Figures 9 and 10). This is expected as the Juno measurements, from which our input MF and SV models were constructed (Sharan, 2023; Sharan et al., 2022a), are closer in radial distance to the northern than to the southern Jovian hemispheres. The difference between the true and predicted SV models (Table 2 and Figures 9 and 10) reflects the performance of different flow solutions in explaining different features of the Jovian SV. The L flow explains more closely the SV in the southern hemisphere than other flows. This can be a sign for the need for flow horizontal divergence there. T flows show zero horizontal divergence everywhere, and the constraints imposed by both TG and CF flows make it very hard to explain some significant horizontal divergence at high latitudes, because of the $\tan\theta$ factor in Equations 17 and 18. Only L flow recovers this SV required feature. Although the L flow gives the smallest SV errors, the strong restriction imposed on small scales is difficult to sustain on physical grounds. Further research on more judicious physical assumptions to use in Jupiter internal flow inversion will be needed in the future.

In this paper we apply an approach commonly used to infer fluid motions at the top of Earth's core (e.g., Finlay et al., 2023; Holme, 2015) to invert for the flow at the top of the dynamo region of Jupiter. However, some fundamental conditions concerning Jupiter's internal structure need to be fulfilled for this approach to be valid. First, the depth at which the dynamo boundary is assumed should not be below the transition between the weakly conducting to the highly conducting layers. In this case, the magnetic field and SV cannot be downward continued as potential fields. Second, the boundary at which we invert for the flow should not reside within the convective region because the radial induction equation that we solve for assumes zero radial velocity there. Our results would be in agreement with an SSL at the top of the dynamo region, and with the steep electrical conductivity transition anywhere within this layer. For instance, for the Earth's core, a stratified layer was proposed at the top of the dynamo region which may extend a few 100s km below the core mantle boundary (CMB) (e.g., Kaneshima, 2018; Pozzo et al., 2012) while core flow inversions reveal the flow just below the CMB (e.g., Finlay et al., 2023; Holme, 2015) where the electrical conductivity transition takes place. For Jupiter, the electrical conductivity transition may reside at different depths depending on the various study techniques. For example, ab-initio simulations place it at 0.9 R_J (French et al., 2012), whereas the magnetic field spectrum becomes flat at $0.81 - 0.83\ R_J$ (Connerney et al., 2022; Sharan et al., 2022a). According to a recent paper by Wulff et al. (2025), the top of the stratified layer can be between 0.83 and 0.89 R_J. Even if the low-to-high electrical conductivity transition is at $\sim$0.9 R_J, it can overlap with the top of the stratified layer, rendering our results plausible. Finally, while different physical constraints for flow inversion should be proposed and tested in the future, our approach brings out a variety of interesting flow structures, which are weakly sensitive to the depth at which the magnetic field and SV models are downward projected.

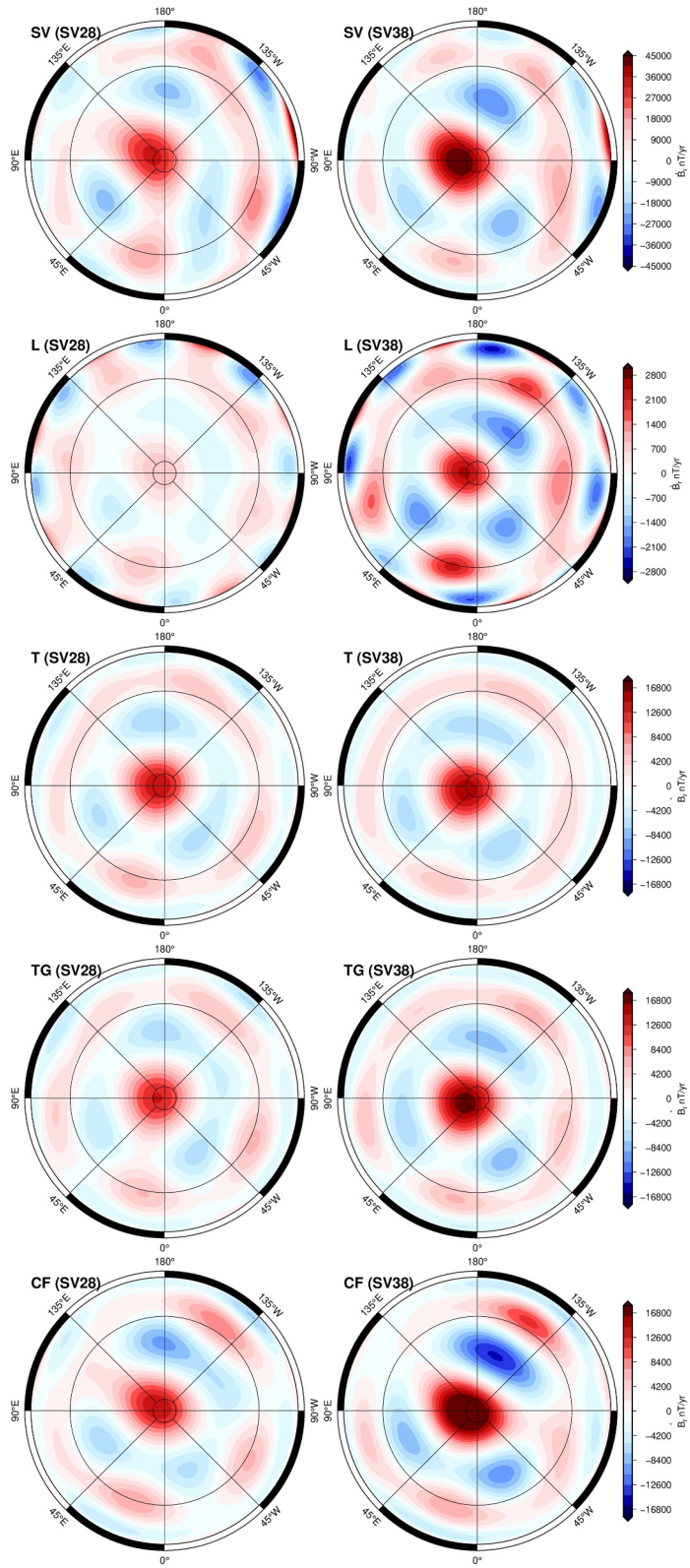

Figure 10. As in Figure 9 but for the south polar view using Orthographic projection. The latitude grid line spacing is 45°.

7. Conclusions

We provide new constraints on Jupiter's internal dynamics starting from two magnetic field models up to degrees 16 (MF) and 8 (SV) (Sharan, 2023; Sharan et al., 2022a) and inverting them to model the flow in the interior up to degree 16. We compute four kinds of solutions, all large-scale, with different physical assumptions: unconstrained L, toroidal T, tangential geostrophic TG and columnar CF flows. Our main findings are:

- We find rich dynamical behavior in the interior of Jupiter, including strong azimuthal flows, upwelling, meridional motions and field-aligned flows.
- While the northern hemisphere and GBS region are dominated by large-scale zonal (eastward) flows, the southern hemisphere is characterized by much smaller scale meridional and non-zonal flows.
- The RMS velocities for all solutions lie between 100 and 400 km/yr at 0.83 R_J, which is our preferred estimate of the Jovian dynamo radius.
- All except L flows reveal a dominant non-zonal component and a striking hemispherical contrast.
- A significant poloidal contribution is present in L flow, to explain the SV near to the south pole as a result of deformation of the field.
- The mean azimuthal (zonal) velocity profiles display peak values near the equatorial region, where strong eastward flow prevails in the GBS region.
- All models are characterized by westward zonal velocities at high latitudes of the southern hemisphere, a possible sign of the thermal wind mechanism acting in the southern hemisphere.
- The L flow displays the smallest SV RMS errors, unsurprisingly as it interacts very weakly with extrapolated small scales of the MF to produce large scale SV.
- Conversely, CF flow displays the highest prediction error, because imposing equatorial symmetry requires more small scale flows.
- T and TG flows explain Jupiter's magnetic data with very similar flows and as a result very similar misfits and modeling errors.
- The two magnetic field models, SV28 and SV38, exhibit large differences in flow magnitude (Table 2), most notably at the equatorial region (Figure 2), demonstrating that refining the MF and SV models is crucial for obtaining more robust models of the flow at the deep interior.

From high resolution magnetic field models, this work allows to investigate and understand several features of the flow present inside Jupiter which govern the field generation. However, some fundamental enigmatic issues concerning the fluid dynamics in the Jovian interior remain unsolved, in particular, the possible need to consider a non-zero radial velocity and the determination of, and dependence on, the dynamo radius. We believe that both our flow solutions and the limitations pointed out in this study can be a motivation for future studies.

Conflict of Interest

The authors declare no conflicts of interest relevant to this study.

Data Availability Statement

The model coefficients for Jupiter's internal field are available at Sharan et al. (2022b) and Sharan (2023).

Acknowledgments
S.S. acknowledges the Imperial Faculty of Natural Sciences (FoNS) postdoc mobility grant for travel to University of Coimbra to carry out part of this work and financial support from the Royal Society Enhancement Grant. M.A.P. acknowledges financial support by Fundação para a Ciência e a Tecnologia (FCT) through the research Grants UIDP/00611/2025 and UIDB/00611/2025. H.A. and B.L. acknowledge financial support from the French Agence Nationale de Recherche, project DYRE-COMB (Grant ANR-22-CE49-0016–01) and Centre National D'Etudes Spatiales (CNES) (support to the JUICE mission). We thank the editor, Beatriz Sanchez-Cano, and two anonymous reviewers for constructive comments which helped improve the manuscript.

References

Amit, H. (2014). Can downwelling at the top of the Earth's core be detected in the geomagnetic secular variation? *Physics of the Earth and Planetary Interiors*, *229*, 110–121. https://doi.org/10.1016/j.pepi.2014.01.012

Amit, H., Coutelier, M., & Christensen, U. R. (2018). On equatorially symmetric and antisymmetric geomagnetic secular variation timescales. *Physics of the Earth and Planetary Interiors*, *276*, 190–201. (Special Issue:15th SEDI conference). https://doi.org/10.1016/j.pepi.2017.04.009

Amit, H., & Olson, P. (2004). Helical core flow from geomagnetic secular variation. *Physics of the Earth and Planetary Interiors*, *147*(1), 1–25. https://doi.org/10.1016/j.pepi.2004.02.006

Amit, H., & Pais, M. A. (2013). Differences between tangential geostrophy and columnar flow. *Geophysical Journal International*, *194*(1), 145–157. https://doi.org/10.1093/gji/ggt077

Bloxham, J., Cao, H., Stevenson, D. J., Connerney, J. E. P., & Bolton, S. J. (2024). A rapidly time-varying equatorial jet in Jupiter's deep interior. *Nature*, *627*(8002), 64–66. https://doi.org/10.1038/s41586-024-07046-3

Bloxham, J., & Jackson, A. (1991). Fluid flow near the surface of Earth's outer core. *Reviews of Geophysics*, *29*(1), 97–120. https://doi.org/10.1029/90rg02470

Bloxham, J., Moore, K. M., Kulowski, L., Cao, H., Yadav, R. K., Stevenson, D. J., et al. (2022). Differential rotation in Jupiter's interior revealed by simultaneous inversion for the magnetic field and zonal flux velocity. *Journal of Geophysical Research: Planets*, *127*(5), e2021JE007138. https://doi.org/10.1029/2021je007138

Bouligand, C., Gillet, N., Jault, D., Schaeffer, N., Fournier, A., & Aubert, J. (2016). Frequency spectrum of the geomagnetic field harmonic coefficients from dynamo simulations. *Geophysical Journal International*, *207*(2), 1142–1157. https://doi.org/10.1093/gji/ggw326

Brygoo, S., Loubeyre, P., Millot, M., Rygg, J. R., Celliers, P. M., Eggert, J. H., et al. (2021). Evidence of hydrogen helium immiscibility at Jupiter interior conditions. *Nature*, *593*(7860), 517–521. https://doi.org/10.1038/s41586-021-03516-0

Busse, F. H. (1975). A model of the geodynamo. *Geophysical Journal of the Royal Astronomical Society*, *42*(2), 437–459. https://doi.org/10.1111/j.1365-246x.1975.tb05871.x

Cao, H., & Stevenson, D. J. (2017). Zonal flow magnetic field interaction in the semi-conducting region of giant planets. *Icarus*, *296*, 59–72. https://doi.org/10.1016/j.icarus.2017.05.015

Christensen, U. R., Aubert, J., & Hulot, G. (2010). Conditions for Earth-like geodynamo models. *Earth and Planetary Science Letters*, *296*(3), 487–496. https://doi.org/10.1016/j.epsl.2010.06.009

Christensen, U. R., & Tilgner, A. (2004). Power requirement of the geodynamo from Ohmic losses in numerical and laboratory dynamos. *Nature*, *429*(6988), 169–171. https://doi.org/10.1038/nature02508

Christensen, U. R., Wardinski, I., & Lesur, V. (2012). Timescales of geomagnetic secular acceleration in satellite field models and geodynamo models. *Geophysical Journal International*, *190*(1), 243–254. https://doi.org/10.1111/j.1365-246X.2012.05508.x

Christensen, U. R., & Wulff, P. N. (2024). Quenching of zonal winds in Jupiter's interior. *Proceedings of the National Academy of Sciences*, *121*(25), e2402859121. https://doi.org/10.1073/pnas.2402859121

Connerney, J. E. P., Timmins, S., Oliversen, R. J., Espley, J. R., Joergensen, J. L., Kotsiaros, S., et al. (2022). A new model of Jupiter's magnetic field at the completion of Juno's prime mission. *Journal of Geophysical Research: Planets*, *127*(2), e2021JE007055. https://doi.org/10.1029/2021je007055

Debras, F., & Chabrier, G. (2019). New models of Jupiter in the context of Juno and Galileo. *The Astrophysical Journal*, *872*(1), 100. https://doi.org/10.3847/1538-4357/aaff65

Eymin, C., & Hulot, G. (2005). On core surface flows inferred from satellite magnetic data. *Physics of the Earth and Planetary Interiors*, *152*(3), 200–220. https://doi.org/10.1016/j.pepi.2005.06.009

Finlay, C. C., & Amit, H. (2011). On flow magnitude and field-flow alignment at Earth's core surface. *Geophysical Journal International*, *186*(1), 175–192. https://doi.org/10.1111/j.1365-246X.2011.05032.x

Finlay, C. C., Dumberry, M., Chulliat, A., & Pais, M. A. (2010). Short timescale core dynamics: Theory and observations. *Space Science Reviews*, *155*, 177–218. https://doi.org/10.1007/978-1-4419-7955-1_8

Finlay, C. C., Gillet, N., Aubert, J., Livermore, P., & Jault, D. (2023). Gyres, jets and waves in Earth's core. *Nature Reviews Earth & Environment*, *4*(6), 377–392. https://doi.org/10.1038/s43017-023-00425-w

French, M., Becker, A., Lorenzen, W., Nettelmann, N., Bethkenhagen, M., Wicht, J., & Redmer, R. (2012). Ab initio simulations for material properties along the Jupiter Adiabat. *The Astrophysical Journal - Supplement Series*, *202*(1), 5. https://doi.org/10.1088/0067-0049/202/1/5

Galanti, E., Kaspi, Y., Duer, K., Fletcher, L., Ingersoll, A. P., Li, C., et al. (2021). Constraints on the latitudinal profile of Jupiter's deep jets. *Geophysical Research Letters*, *48*(9), e2021GL092912. https://doi.org/10.1029/2021gl092912

Gastine, T., & Wicht, J. (2021). Stable stratification promotes multiple zonal jets in a turbulent Jovian dynamo model. *Icarus*, *368*, 114514. https://doi.org/10.1016/j.icarus.2021.114514

Gillet, N., Huder, L., & Aubert, J. (2019). A reduced stochastic model of core surface dynamics based on geodynamo simulations. *Geophysical Journal International*, *219*(1), 522–539. https://doi.org/10.1093/gji/ggz313

Gillet, N., Pais, M. A., & Jault, D. (2009). Ensemble inversion of time-dependent core flow models. *Geochemistry, Geophysics, Geosystems*, *10*(6). https://doi.org/10.1029/2008gc002290

Gillet, N., Schaeffer, N., & Jault, D. (2011). Rationale and geophysical evidence for quasi-geostrophic rapid dynamics within the Earth's outer core. *Physics of the Earth and Planetary Interiors*, *187*(3–4), 380–390. https://doi.org/10.1016/j.pepi.2011.01.005

Holme, R. (2015). Large-scale flow in the core. *Treatise on Geophysics*, 91–113. https://doi.org/10.1016/B978-0-444-53802-4.00138-X

Hulot, G., Eymin, C., Langlais, B., Mandea, M., & Olsen, N. (2002). Small-scale structure of the geodynamo inferred from Oersted and Magsat satellite data. *Nature*, *416*(6881), 620–623. https://doi.org/10.1038/416620a

Jackson, A., & Finlay, C. C. (2007). Geomagnetic secular variation and its applications to the core. In G. Schubert (Ed.) (Vol. *5*, pp. 147–193). https://doi.org/10.1016/B978-044452748-6.00090-0

Kaneshima, S. (2018). Array analyses of SmKS waves and the stratification of Earth's outermost core. *Physics of the Earth and Planetary Interiors*, *276*, 234–246. https://doi.org/10.1016/j.pepi.2017.03.006

Kaspi, Y., Galanti, E., Hubbard, W. B., Stevenson, D. J., Bolton, S. J., Iess, L., et al. (2018). Jupiter's atmospheric jet streams extend thousands of Kilometres deep. *Nature*, *555*(7695), 223–226. https://doi.org/10.1038/nature25793

Langlais, B., Amit, H., Larnier, H., Thébault, E., & Mocquet, A. (2014). A new model for the (geo)magnetic power spectrum, with application to planetary dynamo radii. *Earth and Planetary Science Letters*, *401*, 347–358. https://doi.org/10.1016/j.epsl.2014.05.013

Le Mouël, J. L. (1984). Outer-core geostrophic flow and secular variation of Earth's geomagnetic field. *Nature*, *311*(5988), 734–735. https://doi.org/10.1038/311734a0

Lesur, V., Gillet, N., Hammer, M. D., & Mandea, M. (2022). Rapid variations of Earth's core magnetic field. *Surveys in Geophysics*, *43*(1), 41–69. https://doi.org/10.1007/s10712-021-09662-4

Lézin, M., Amit, H., Terra-Nova, F., & Wardinski, I. (2023). Mantle-driven north–south dichotomy in geomagnetic polar minima. *Physics of the Earth and Planetary Interiors*, *337*, 107000. https://doi.org/10.1016/j.pepi.2023.107000

Lhuillier, F., Fournier, A., Hulot, G., & Aubert, J. (2011). The geomagnetic secular-variation timescale in observations and numerical dynamo models. *Geophysical Research Letters*, *38*(9). https://doi.org/10.1029/2011GL047356

Militzer, B., & Hubbard, W. B. (2023). Relation of gravity, winds, and the moment of inertia of Jupiter and Saturn. *The Planetary Science Journal*, *4*(5), 95. https://doi.org/10.3847/psj/acd2cd

Moore, K. M., Barik, A., Stanley, S., Stevenson, D. J., Nettelmann, N., Helled, R., et al. (2022). Dynamo simulations of Jupiter's magnetic field: The role of stable stratification and a dilute core. *Journal of Geophysical Research: Planets*, *127*(11), e2022JE007479. https://doi.org/10.1029/2022je007479

Moore, K. M., Cao, H., Bloxham, J., Stevenson, D. J., Connerney, J. E. P., & Bolton, S. J. (2019). Time variation of Jupiter's internal magnetic field consistent with zonal wind advection. *Nature Astronomy*, *3*(8), 730–735. https://doi.org/10.1038/s41550-019-0772-5

Mound, J., Davies, C., Rost, S., & Aurnou, J. (2019). Regional stratification at the top of Earth's core due to core-mantle boundary heat flux variations. *Nature Geoscience*, *12*(7), 575–580. https://doi.org/10.1038/s41561-019-0381-z

Olson, P., & Aurnou, J. (1999). A polar vortex in the Earth's core. *Nature*, *402*(6758), 170–173. https://doi.org/10.1038/46017

Olson, P., Landeau, M., & Reynolds, E. (2017). Dynamo tests for stratification below the core-mantle boundary. *Physics of the Earth and Planetary Interiors*, *271*, 1–18. https://doi.org/10.1016/j.pepi.2017.07.003

Pais, M. A., & Jault, D. (2008). Quasi-geostrophic flows responsible for the secular variation of the Earth's magnetic field. *Geophysical Journal International*, *173*(2), 421–443. https://doi.org/10.1111/j.1365-246x.2008.03741.x

Pais, M. A., Morozova, A. L., & Schaeffer, N. (2014). Variability modes in core flows inverted from geomagnetic field models. *Geophysical Journal International*, *200*(1), 402–420. https://doi.org/10.1093/gji/ggu403

Pais, M. A., Oliveira, O., & Nogueira, F. (2004). Nonuniqueness of inverted core-mantle boundary flows and deviations from tangential geostrophy. *Journal of Geophysical Research*, *109*(B8). https://doi.org/10.1029/2004jb003012

Porco, C. C., West, R. A., McEwen, A., Del Genio, A. D., Ingersoll, A. P., Thomas, P., et al. (2003). Cassini imaging of Jupiter's atmosphere, satellites, and rings. *Science*, *299*(5612), 1541–1547. https://doi.org/10.1126/science.1079462

Pozzo, M., Davies, C., Gubbins, D., & Alfe, D. (2012). Thermal and electrical conductivity of iron at Earth's core conditions. *Nature*, *485*(7398), 355–358. https://doi.org/10.1038/nature11031

Ridley, V. A., & Holme, R. (2016). Modeling the Jovian magnetic field and its secular variation using all available magnetic field observations. *Journal of Geophysical Research: Planets*, *121*(3), 309–337. https://doi.org/10.1002/2015JE004951

Roberts, P. H., & Scott, S. (1965). On analysis of the secular variation 1. A hydromagnetic constraint: Theory. *Journal of Geomagnetism and Geoelectricity*, *17*(2), 137–151.

Schaeffer, N., Jault, D., Nataf, H. C., & Fournier, A. (2017). Turbulent geodynamo simulations: A leap towards Earth's core. *Geophysical Journal International*, *211*(1), 1–29. https://doi.org/10.1093/gji/ggx265

Sharan, S. (2023). *The interior of planets as characterised by their magnetic fields: The Jovian and Martian cases*. Theses, Nantes Université). Retrieved from https://theses.hal.science/tel-04624352/file/SHARAN.pdf

Sharan, S., Langlais, B., Amit, H., Thébault, E., Pinceloup, M., & Verhoeven, O. (2022a). The internal structure and dynamics of Jupiter unveiled by a high-resolution magnetic field and secular variation model. *Geophysical Research Letters*, *49*(15), e2022GL098839. https://doi.org/10.1029/2022gl098839

Sharan, S., Langlais, B., Amit, H., Thébault, E., Pinceloup, M., & Verhoeven, O. (2022b). Spherical harmonic model of Jupiter's magnetic field and secular variation [Dataset]. *Zenodo*. https://doi.org/10.5281/zenodo.6564162

Simon, A. A., Wong, M. H., & Orton, G. S. (2015). First results from the Hubble OPAL program: Jupiter in 2015. *The Astrophysical Journal*, *812*(1), 55. https://doi.org/10.1088/0004-637x/812/1/55

Simon-Miller, A. A., & Gierasch, P. J. (2010). On the long-term variability of Jupiter's winds and brightness as observed from Hubble. *Icarus*, *210*(1), 258–269. https://doi.org/10.1016/j.icarus.2010.06.020

Terra-Nova, F., & Amit, H. (2024). Regionally-triggered geomagnetic reversals. *Scientific Reports*, *14*(1), 9639. https://doi.org/10.1038/s41598-024-59849-z

Tsang, Y.-K., & Jones, C. A. (2020). Characterising Jupiter's dynamo radius using its magnetic energy spectrum. *Earth and Planetary Science Letters*, *530*, 115879. https://doi.org/10.1016/j.epsl.2019.115879

Whaler, K. A. (1980). Does the whole of the Earth's core convect? *Nature*, *287*(5782), 528–530. https://doi.org/10.1038/287528a0

Wicht, J., & Christensen, U. R. (2024). Contributions of Jupiter's deep-reaching surface winds to magnetic field structure and secular variation. *Journal of Geophysical Research: Planets*, *129*(4), e2023JE007890. https://doi.org/10.1029/2023je007890

Wicht, J., & Gastine, T. (2020). Numerical simulations help revealing the dynamics underneath the clouds of Jupiter. *Nature Communications*, *11*(1), 2886. https://doi.org/10.1038/s41467-020-16680-0

Wicht, J., Gastine, T., & Duarte, L. D. V. (2019). Dynamo action in the steeply decaying conductivity region of jupiter-like dynamo models. *Journal of Geophysical Research: Planets*, *124*(3), 837–863. https://doi.org/10.1029/2018JE005759

Wulff, P. N., Cao, H., & Aurnou, J. M. (2025). On the meaning of the dynamo radius in giant planets with stable layer. *The Astrophysical Journal*, *992*(1), 50. https://doi.org/10.3847/1538-4357/adf736

Wulff, P. N., Dietrich, W., Christensen, U. R., & Wicht, J. (2022). Zonal winds in the gas planets driven by convection above a stably stratified layer. *Monthly Notices of the Royal Astronomical Society*, *517*(4), 5584–5593. https://doi.org/10.1093/mnras/stac3045